REPORT DOCUMENTATION PAGE

Form Approved OMB NO. 0704-0188

1. REPORT DATE (DD-MM-YYYY)	2. REPORT TYPE	3. DATES COVERED (From - To)
08-03-2019	Final Report	21-Aug-2015 - 20-Aug-2018

4. TITLE AND SUBTITLE
Final Report: High-Speed Blue and Green Light-Emitting Diodes Using Polarization-Free GaN

5a. CONTRACT NUMBER
W911NF-15-1-0428

5b. GRANT NUMBER

5c. PROGRAM ELEMENT NUMBER
106012

6. AUTHORS

5d. PROJECT NUMBER

5e. TASK NUMBER

5f. WORK UNIT NUMBER

7. PERFORMING ORGANIZATION NAMES AND ADDRESSES
University of New Mexico Albuquerque
1700 Lomas Boulevard NE, Suite 2200, MSC01 1247
1 University of New Mexico
Albuquerque, NM 87131 -0001

8. PERFORMING ORGANIZATION REPORT NUMBER

9. SPONSORING/MONITORING AGENCY NAME(S) AND ADDRESS (ES)
U.S. Army Research Office
P.O. Box 12211
Research Triangle Park, NC 27709-2211

10. SPONSOR/MONITOR'S ACRONYM(S)
ARO

11. SPONSOR/MONITOR'S REPORT NUMBER(S)
67348-EL-REP.26

12. DISTRIBUTION AVAILIBILITY STATEMENT
Approved for public release; distribution is unlimited.

13. SUPPLEMENTARY NOTES
The views, opinions and/or findings contained in this report are those of the author(s) and should not contrued as an official Department of the Army position, policy or decision, unless so designated by other documentation.

14. ABSTRACT

15. SUBJECT TERMS

16. SECURITY CLASSIFICATION OF:			17. LIMITATION OF ABSTRACT	15. NUMBER OF PAGES	19a. NAME OF RESPONSIBLE PERSON
a. REPORT	b. ABSTRACT	c. THIS PAGE			Daniel Feezell
UU	UU	UU	UU		19b. TELEPHONE NUMBER 505-272-7800

RPPR Final Report
as of 18-Mar-2019

Agency Code:

Proposal Number: 67348ELREP **Agreement Number: W911NF-15-1-0428**
INVESTIGATOR(S):

Name: Daniel Feezell
Email: dfeezell@unm.edu
Phone Number: 5052727800
Principal: Y

Organization: **University of New Mexico Albuquerque**
Address: 1700 Lomas Boulevard NE, Suite 2200, MSC01 1247, Albuquerque, NM 871310001
Country: USA

DUNS Number: 868853094 EIN: 856000642
Report Date: 20-Nov-2018 Date Received: 08-Mar-2019
Final Report for Period Beginning 21-Aug-2015 and Ending 20-Aug-2018
Title: High-Speed Blue and Green Light-Emitting Diodes Using Polarization-Free GaN
Begin Performance Period: 21-Aug-2015 **End Performance Period:** 20-Aug-2018
Report Term: 0-Other

Submitted By: Daniel Feezell Email: dfeezell@unm.edu
Phone: (505) 272-7800

Distribution Statement: 1-Approved for public release; distribution is unlimited.

STEM Degrees: 1 **STEM Participants:** 1

Major Goals: The primary goal of this project is to develop high-speed nonpolar and semipolar blue and green light-emitting diodes (LEDs) with applications to underwater optical communication. The blue devices will emit near 430-450 nm and the green devices will emit near 500-520 nm. The devices will be grown on nonpolar (10-10) substrates and the semipolar devices will be grown on (20-2-1) substrates. The main goal for high speed performance is to realize bandwidths beyond 1 GHz. The tasks are divided into the following four thrusts.

A. LED design
A.1 Design of LED active regions using simulation and experiment
A.2 Design of geometry and layer thickness for a vertical LED
A.3 Photomask layout for individual LEDs and arrays

B. Epitaxial materials growth
B.1 Optimization of nonpolar (10-10) LED structures
B.2 Optimization of semipolar (20-2-1) LED structures
B.3 Growth of test structures for optimization of series resistance, capacitance, doping, etc.

C. LED fabrication
C.1 Individual vertical LED fabrication
C.2 LED array fabrication

D. LED and materials characterization.
D.1 DC characterization of the LEDs
D.2 RF small-signal characterization of the LEDs
D.3 TRPL lifetime measurements

The completion criteria for each task, the target completion quarter, and the estimated completion percentage for each task are given below. Most tasks have been 100% completed upon the completion of the three-year program.

A.1 Variety of structures simulated, band diagrams produced, and test structures verified (target = Q6, 100%)
We have completed several design optimizations including single and multiple quantum well designs, new designs and optimizations (such as barrier thickness and number of QW optimizations), and designs on two different orientations.

RPPR Final Report
as of 18-Mar-2019

A.2 Epitaxial layer structures designed, device geometry selected (target = Q2, 100%)
Several LED epitaxial designs were produced and investigated.

A.3 Photomasks drawn, ordered, and received from vendor (target = Q8, 100%)
Two mask design evolutions were developed to resolve issues related to heat-dissipation, RC parasitic components, etc.

B.1 Nonpolar (10-10) LEDs with 50% EQE, forward voltage below 4V at 20 mA, and wavelength ~450 nm (target = Q8, 75%) We have established growth capabilities for nonpolar LEDs and are working to improve the EQE and voltage. Voltage below 4 V at 20 mA was achieved but EQE of more than 50% was not achieved, although output powers in the range of several mW were ahchieved. However, the high-speed performance of the devices was not affected by having an EQE lower than 50%, so this task did not limit the scope of the work performed.

B.2 Semipolar (20-2-1) LEDs with 25% EQE, forward voltage below 4V at 20 mA, and wavelength ~520 nm (target = Q12, 50%) We have established growth capabilities for semipolar LEDs and are working to improve the EQE and voltage. Our semipolar growth is not as mature as our nonpolar growth at this point but we are going to work on it. However, we have demonstrated excellent devices on semipolar (20-2-1) in collaboration with UCSB. UNM has designed, fabricated, and performed PL and RF characterization on UCSB material with excellent results. These materials have EQEs of more than 25%, but are emitting near 450 nm.

B.3 TLMs fabricated and measured, p-GaN resistivity ~2 ohm-cm, capacitance minimized, effects of doping on resistance explored (target = Q4, 100%) Many test structures have been produced and measured. We optimized p-GaN and n-GaN growth conditions. We worked on minimizing the resistance and capacitance and reducing ICP damage of the epi-layers by optimizing etching conditions in year 3.

C.1 Vertical LEDs fabricated on nonpolar and semipolar substrates (target = Q8, 100%) We proposed to modify the vertical LED design in the proposal to a co-planar horizontal LED design. This modification is necessitated by the device geometry required to perform the RF testing using the RF probe station we have available. We have fabricated various LED designs and optimized fabrication steps in years 2 and 3.

C.2 Vertical LED arrays fabricated on nonpolar and semipolar substrates (target = Q8, 75%)
In this year, we did the first demonstration of LED arrays and tested electrically for both series and parallel designs. Arrays of LEDs were produced on both nonpolar and semipolar substrates. However, the individual LED pixels were not yet electrically connected at the conclusion of year 3.

D.1 LOP, IV, EQE, wavelength, hot/cold factor, etc. measured (target = Q12, 100%)
These measurements have been performed for various LED designs in years 1 and 2 and 3.

D.2 RF modulation bandwidth measured for a variety of device designs and operating conditions (target = Q12, 100%) Not only have we performed various RF small-signal testing of semipolar and nonpolar devices and published several journal papers, but also we developed a small-signal circuit model to account for various recombination and injection processes within the LED active regions using the RF setup. Using such models we can design and implement devices with faster modulation response and higher efficiency. We also built a pulsed RF set up to decouple effects of heating on LED performance. The pulsed RF set up was used to decouple the effects of heating and injection from the LEDs. We identified the origins of efficiency and thermal droop in some of our LED using the pulsed RF set up.

D.3 Carrier lifetime extracted on bare material for nonpolar and semipolar and correlated to bandwidth measurements (target = Q12, 100%) We have performed TRPL on semipolar and nonpolar LEDs and compared the lifetimes (actual lifetime or ?_n) with those obtained from bandwidth measurements (differential lifetime or ?_?n). We also discussed the differences between the measured lifetimes using optical and electrical techniques and their physical significance. Extensive electrically injected lifetime measurements were performed and correlated with the TRPL results.

Accomplishments: The detailed technical accomplishments for the project are given in the 52-page pdf document included under the Upload Report Attachment option. In this section, these accomplishments are briefly summarized due to space constraints.

Key accomplishment highlights include:

RPPR Final Report
as of 18-Mar-2019

1. We presented a world record modulation bandwidth of 1.3 to 1.5 GHz at low current densities (200-500 A/cm2). Previously, the highest reported modulation bandwidths related to c-plane LEDs were up to a GHz at 5-10 kA/cm2.

2. For the first time, we performed a comparison of bandwidth vs. current density for nonpolar, semipolar and polar orientations. The study revealed that due to lack of QCSE in nonpolar, we can obtain GHz bandwidth at very low current densities (~ 100 A/cm2) where efficiency droop, thermal droop, and power consumption is minimized which results in a higher BEFOM for nonpolar LEDs.

3. A rate-equation-based modeling to account for carrier dynamics in InGaN/GaN LEDs under electrical injection was developed throughout the project. We were able to obtain various recombination and escape rates by simultaneous fitting of RF data (impedance and S21).

4. We developed the first pulsed-RF measurement setup to study carrier dynamics under isothermal condition.

5. We evaluated the recombination coefficients of semipolar InGaN/GaN LEDs using a differential lifetime analysis based on our RF measurement tool. The study revealed that low auger coefficient (C) is responsible for the observed lower droop in the semipolar LED compared to c-plane LED.

6. A systematic evaluation of recombination rates using our developed rate-equation based modeling under isothermal condition revealed the cause of efficiency and thermal droop in InGaN/GaN LEDs which had been subject of debate in the past decades. We were also able to determine the injection efficiency and corresponding radiative efficiency of InGaN/GaN LEDs using our rate-equation based modeling. Our findings excluded the injection efficiency as the primary cause of efficiency droop.

7. We explored the trade-off between modulation bandwidth and efficiency of InGaN/GaN LEDs for the first time. We suggested a figure of merit that accounts for both bandwidth and efficiency (BEFOM as described in section 4) for dual illumination and communication applications. Our study develops a platform to understand various mechanisms responsible for bandwidth/efficiency limitations at different current density ranges which allows for co-optimization of bandwidth and efficiency in InGaN/LEDs for VLC.

8. One student (Dr. Arman Rashidi) received his Ph.D. working entirely on this funded DOD project.

9. We published eight journal articles, with one more under review, and a comprehensive review of the field under preparation for Laser and Photonics Reviews. We also gave more than 11 conference presentations, with six of these as invited talks. Dr. Rashidi also gave a TED talk on the project.

Training Opportunities: There were several training activities that were performed during the project. Two of the graduate students working on this project (Mr. Andrew Aragon and Mr. Arman Rashidi) were involved in mentoring an undergraduate student (Ms. Olivia Johnson) in activities related to the project, including device testing, growth, and fabrication. Ms. Johnson has worked on the project for the full second year and has graduated from UNM and is now working in the commercial sector at the Palo Verde Nuclear Generating Station. While at UNM, she attended weekly group meetings discussing the project and received one-on-one mentoring from the PI and the graduate students working on the project. The PI is also involved in directly training the graduate students on design, growth, fabrication, and characterization techniques. Moreover, the graduate students both participate in weekly group meetings to discuss the project and perform their own individual study throughout the week. One of the graduate students (Mr. Arman Rashidi) has presented his work related to this project at four conferences. The postdoctoral researcher assisting with this project gave three conference presentations. The PI gave six invited talks on the work from this project. The PI also presented at the Illuminating Engineering Society monthly meeting in Albuquerque, where results were disseminated to a public audience of about 50 people.

Finally, Dr. Arman Rashidi received his Ph.D performing work on this project. Dr. Rashidi graduated with distinction from the University of New Mexico in the Optical Science and Engineering program. Dr. Rashidi also gave a Technology, Entertainment, and Design talk on visible light communication where he referenced the work from this project. Dr. Rashidi also received the "Best Student Presentation" award at the 2018 Lester Eastman Conference.

RPPR Final Report
as of 18-Mar-2019

Results Dissemination: We have several papers published in high impact journals based on the work from this project. Each paper acknowledges support form W911NF1510428. We have also published the results at more than 11 conferences. The list of journal, conference, and other publications is given below:
Journals:

1. A. Rashidi, M. Monavarian, A. Aragon, S. Okur, M. Nami, A. Rishinaramangalam, S. Mishkat-Ul-Masabih, D. Feezell, “High-Speed Nonpolar InGaN/GaN LEDs for Visible-Light Communication”, IEEE Photonics Technology Letters, Vol. 29, No. 4 (2017).

2. S. Okur, M. Nami, A. Rishinaramangalam, S. H. Oh, S. P. DenBaars, S. Liu, I. Brener, and D. Feezell, “Internal quantum efficiency and carrier dynamics in semipolar (20-2-1) InGaN/GaN light-emitting diodes”, Optics Express 25, 2178 (2017).

3. M. Monavarian, A. Rashidi, A. Aragon, S. H. Oh, M. Nami, S. P. DenBaars, D. Feezell, “Explanation of low efficiency droop in semipolar (20-2-1) InGaN/GaN LEDs through evaluation of carrier recombination coefficients”, Optics Express 25, 19343 (2017).

4. A. Rashidi, M. Nami, M. Monavarian, A. Aragon, K. DaVico, F. Ayoub, S. Mishkat-Ul-Masabih, A. Rishinaramangalam, D. Feezell, “Differential carrier lifetime and transport effects in electrically injected IIInitride light-emitting diodes”, Journal of Applied Physics 122, 035706 (2017).

5. M. Monavarian, A. Aragon, A. Rashidi, A. Rishinaramangalam, and D. Feezell, “Impact of Crystal Orientation on Modulation Bandwidth of InGaN/GaN Light-Emitting Diodes,” Applied Physics Letters, vol. 112, pp. 041104(1-4), Jan. 2018. doi: 10.1063/1.5019730

6. A. Rashidi, M. Monavarian, A. Aragon, A. Rishinaramangalam, and D. Feezell, “Nonpolar m-Plane InGaN/GaN Micro-Scale Light-Emitting Diode with 1.5 GHz Modulation Bandwidth,” Electron Device Letters, vol. 39, pp. 520 – 523, Mar. 2018. doi: 10.1109/LED.2018.2803082

7. M. Monavarian, A. Rashidi, A. Aragon, M. Nami, S. H. Oh, S. P. DenBaars, and D. Feezell, “Trade-Off Between Bandwidth and Efficiency in Semipolar (202 ?1 ?) InGaN/GaN Single- and Multiple-Quantum-Well Light-Emitting Diodes,” Applied Physics Letters, vol. 112, pp. 191102, May 2018. doi: 10.1063/1.5032115

8. A. Rashidi, M. Monavarian, A. Aragon, M. Nami, A. Rishinaramangalam, and D. Feezell, “Exclusion of Injection Efficiency as the Primary Cause of Efficiency Droop in Semipolar (202 ?1 ?) InGaN/GaN Light-Emitting Diodes,” Applied Physics Letters, vol. 113, pp. 031101, July 2018. doi: 10.1063/1.5036761

Invited Conference Presentations:
1. D. Feezell, “High-Speed GaN-Based Optoelectronics,” 77th Device Research Conference (DRC), Ann Arbor, MI, June 2019.

2. D. Feezell, “Novel measurements and models for understanding the efficacy versus luminance trade-off,” DOE Solid-State Lighting R&D Workshop, Dallas, TX, Jan. 2019. (Invited Panel Speaker)

3. D. Feezell, M. Monavarian, A. Rashidi, M. Nami, and A. Aragon, “High-Speed GaN-Based Micro-Scale Light-Emitting Diodes for Visible-Light Communication,” 234th Meeting of the Electrochemical Society (ECS) – Americas International Meeting on Electrochemistry and Solid-State Science, Cancun, Mexico, Oct. 2018.

4. D. Feezell, M. Monavarian, A. Rashidi, M. Nami, and A. Aragon, “High-Speed GaN-Based Micro-Scale Light-Emitting Diodes for Visible-Light Communication,” SPIE Optics + Photonics Conference, Proc. SPIE, 1075407, San Diego, CA, Sep. 2018. Doi: 10.1117/12.2323266

5. D. Feezell, A. Rashidi, M. Monavarian, M. Nami, and A. Aragon, “High-Speed Nonpolar and Semipolar Light-Emitting Diodes for Visible Light Communication,” Lester Eastman Conference, Columbus, OH, Aug. 2018.

6. D. Feezell, A. Rashidi, M. Monavarian, and A. Aragon, “High-Speed Nonpolar and Semipolar Light-Emitting Diodes for Visible Light Communication,” International Symposium on Advanced Plasma Science and its Applications for Nitrides and Nanomaterials (ISPlasma), Nagoya, Japan, March 2018.

Contributed Conference Presentations:
1. A. Rashidi, M. Monavarian, A. Aragon, A. Rishinaramangalam, D. Feezell, “GHz-bandwidth nonpolar InGaN/GaN micro-LED operating at low current density for visible-light communication,” IEEE International Semiconductor Laser Conference, Santa Fe, NM, Sep. 2018.

2. A. Rashidi, M. Monavarian, A. Aragon, D. Feezell, “Exclusion of injection efficiency as the primary cause of efficiency droop in InGaN/GaN light-emitting diodes,” Lester Eastman Conference, Columbus, OH, Aug. 2018. (winner of Best Student Presentation)

3. A. Rashidi, M. Monavarian, A. Aragon, A. Rishinaramangalam, and D. Feezell, “Carrier Dynamics in High-Speed III-Nitride Light-Emitting Diodes for Visible-Light Communication,” Electronic Materials Conference, Santa Barbara, CA, June 2018.

4. M. Monavarian, A. Rashidi, A. Aragon, A. Rishinaramangalam, S. H. Oh, S. DenBaars, and D. Feezell, “Orientation-dependent modulation response of high-speed InGaN/GaN blue light-emitting diodes for visible-light communication,” Compound Semiconductor Week, Boston, MA, June 2018.

5. A. Rashidi, M. Monavarian, A. Aragon, S. Okur, M. Nami, A. Rishinaramangalam, S. Mishkat-Ul-Masabih, D. Feezell, “High-Speed Nonpolar InGaN/GaN LEDs for Visible-Light Communication,” 2017 Conference on Lasers and Electro-Optics (CLEO), San Jose, CA, May 2017.

Other presentations related to the project:
1. D. Feezell, “High-Speed Micro-Scale Light-Emitting Diodes for Visible-Light Communication,” University of Utah, Salt Lake City, UT, Feb. 2019.

2. D. Feezell, “Novel measurements and models for understanding the efficacy versus luminance trade-off,” DOE Solid-State Lighting R&D Workshop, Dallas, TX, Jan. 2019. (Invited Panel Speaker)

3. D. Feezell, “High-Speed Micro-Scale Light-Emitting Diodes for Visible-Light Communication,” Illuminating Engineering Society, Albuquerque Chapter, Jan. 2018.

4. Dr. Arman Rashidi gave a TED talk

Honors and Awards: 1. Dr. Arman Rashidi won the Best Student Presentation award at the 2018 Lester Eastman conference for his talk “Exclusion of injection efficiency as the primary cause of efficiency droop in InGaN/GaN light-emitting diodes.”

2. Dr. Arman Rashidi graduated with distinction for his Ph.D. dissertation titled, "Carrier Dynamics in High-Speed III-Nitride Light-Emitting Diodes for Visible-Light Communication"

3. Our paper “Explanation of low efficiency droop in semipolar (20-2-1) InGaN/GaN LEDs through evaluation of carrier recombination coefficients”, Optics Express 25, 19343 (2017) received Editors Pick in Optics Express.

4 Our paper “Impact of crystal orientation on the modulation bandwidth of InGaN/GaN light-emitting diodes” was a Top 20 Most Cited Papers in Applied Physics Letters in 2018.

5. Our paper “Impact of crystal orientation on the modulation bandwidth of InGaN/GaN light-emitting diodes” was featured in Semiconductor Today magazine.

Protocol Activity Status:

Technology Transfer: Nothing to Report

PARTICIPANTS:

Participant Type: PD/PI
Participant: Daniel Feezell

Person Months Worked: 1.00 **Funding Support:**
Project Contribution:
International Collaboration:
International Travel:
National Academy Member: N
Other Collaborators:

Participant Type: Graduate Student (research assistant)
Participant: Arman Rashidi
Person Months Worked: 6.00 **Funding Support:**
Project Contribution:
International Collaboration:
International Travel:
National Academy Member: N
Other Collaborators:

Participant Type: Graduate Student (research assistant)
Participant: Arman Rashidi
Person Months Worked: 6.00 **Funding Support:**
Project Contribution:
International Collaboration:
International Travel:
National Academy Member: N
Other Collaborators:

Participant Type: Postdoctoral (scholar, fellow or other postdoctoral position)
Participant: Morteza Monavarian
Person Months Worked: 4.00 **Funding Support:**
Project Contribution:
International Collaboration:
International Travel:
National Academy Member: N
Other Collaborators:

Participant Type: Undergraduate Student
Participant: Neema Naieemi
Person Months Worked: 3.00 **Funding Support:**
Project Contribution:
International Collaboration:
International Travel:
National Academy Member: N
Other Collaborators:

CONFERENCE PAPERS:

RPPR Final Report
as of 18-Mar-2019

Publication Type: Conference Paper or Presentation **Publication Status:** 1-Published
Conference Name: Conference on Lasers and Electro-Optics
Date Received: 01-Aug-2017 Conference Date: 18-May-2017 Date Published: 18-May-2017
Conference Location: San Jose, CA
Paper Title: High-Speed Nonpolar InGaN/GaN LEDs for Visible-Light Communication
Authors: Arman Rashidi, Morteza Monavarian, Andrew Aragon, Serdal Okur, Mohsen Nami, Ashwin Rishinarama
Acknowledged Federal Support: **Y**

Publication Type: Conference Paper or Presentation **Publication Status:** 1-Published
Conference Name: 234th Meeting of the Electrochemical Society (ECS) – Americas International Meeting on Electrochemistry and Solid-State Science
Date Received: 08-Mar-2019 Conference Date: 02-Oct-2018 Date Published: 09-Oct-2018
Conference Location: Cancun, Mexico
Paper Title: High-Speed GaN-Based Micro-Scale Light-Emitting Diodes for Visible-Light Communication
Authors: D. Feezell, M. Monavarian, A. Rashidi, M. Nami, and A. Aragon
Acknowledged Federal Support: **Y**

Publication Type: Conference Paper or Presentation **Publication Status:** 1-Published
Conference Name: Wide Bandgap Power and Energy Devices and Applications III
Date Received: 08-Mar-2019 Conference Date: 19-Aug-2018 Date Published:
Conference Location: San Diego, United States
Paper Title: High-speed GaN-based micro-scale light-emitting diodes for visible-light communication (Conference Presentation)
Authors: D. Feezell, M. Monavarian, A. Rashidi, M. Nami, and A. Aragon
Acknowledged Federal Support: **Y**

Publication Type: Conference Paper or Presentation **Publication Status:** 1-Published
Conference Name: Lester Eastman Conference
Date Received: 08-Mar-2019 Conference Date: 09-Mar-2018 Date Published:
Conference Location: Columbus, OH
Paper Title: High-Speed Nonpolar and Semipolar Light-Emitting Diodes for Visible Light Communication
Authors: D. Feezell, A. Rashidi, M. Monavarian, M. Nami, and A. Aragon
Acknowledged Federal Support: **Y**

Publication Type: Conference Paper or Presentation **Publication Status:** 1-Published
Conference Name: International Symposium on Advanced Plasma Science and its Applications for Nitrides and Nanomaterials (ISPlasma)
Date Received: 08-Mar-2019 Conference Date: 09-Mar-2018 Date Published:
Conference Location: Nagoya, Japan
Paper Title: High-Speed Nonpolar and Semipolar Light-Emitting Diodes for Visible Light Communication
Authors: D. Feezell, A. Rashidi, M. Monavarian, and A. Aragon
Acknowledged Federal Support: **Y**

Publication Type: Conference Paper or Presentation **Publication Status:** 1-Published
Conference Name: 2018 IEEE International Semiconductor Laser Conference (ISLC)
Date Received: 08-Mar-2019 Conference Date: 16-Sep-2018 Date Published:
Conference Location: Santa Fe, NM
Paper Title: GHz-Bandwidth Nonpolar InGaN/GaN Micro-LED Operating at Low Current Density for Visible-Light Communication
Authors: A. Rashidi, M. Monavarian, A. Aragon, A. Rishinaramangalam, D. Feezell
Acknowledged Federal Support: **Y**

RPPR Final Report
as of 18-Mar-2019

Publication Type: Conference Paper or Presentation **Publication Status:** 1-Published
Conference Name: Compound Semiconductor Week
Date Received: 08-Mar-2019 Conference Date: 30-May-2018 Date Published:
Conference Location: Boston, MA
Paper Title: Orientation-dependent modulation response of high-speed InGaN/GaN blue light-emitting diodes for visible-light communication
Authors: M. Monavarian, A. Rashidi, A. Aragon, A. Rishinaramangalam, S. H. Oh, S. DenBaars, and D. Feezell
Acknowledged Federal Support: **Y**

DISSERTATIONS:

Publication Type: Thesis or Dissertation
Institution: University of New Mexico
Date Received: 08-Mar-2019 Completion Date: 12/2/18 11:49AM
Title: CARRIER DYNAMICS IN HIGH-SPEED III-NITRIDE LIGHT-EMITTING DIODES FOR VISIBLE-LIGHT COMMUNICATION
Authors: Arman, Rashidi
Acknowledged Federal Support: **N**

High-Speed Blue and Green Light-Emitting Diodes Using Polarization-Free GaN

Final Report

Proposal Number: 67348-EL-REP

Agreement Number: W911NF1510428

Reporting Period: 8/31/17 – 7/31/18

PI: Daniel Feezell

Center for High Technology Materials (CHTM), The University of New Mexico, Albuquerque, NM 87106, USA

1. Introduction

High-speed InGaN/GaN light-emitting diodes (LEDs) have recently been of great interest for applications in visible-light communication (VLC), short-range underwater wireless optical communication (UWOC), and plastic optical fiber (POF) communication.[1] Although diode lasers can achieve higher modulation bandwidths than LEDs, LEDs remain of interest for communications due to their low cost, low power consumption, and compatibility with current solid state lighting systems[2,3]. Development of high-speed InGaN/GaN LEDs on *c*-plane GaN on sapphire has progressed from tens of MHz to more than 800 MHz over a period of more than ten years[4–7]. These advancements have been enabled by improvements in active region design, device architecture, and thermal management. One challenge limiting further improvement of the modulation bandwidth in *c*-plane LEDs is the presence of polarization-related electric fields, which separate the electron and hole wave functions in the active region[8] and increase the carrier lifetime[9].

Semipolar and nonpolar choices of substrate orientations could be of greater interests due to faster recombination lifetimes[10,11] which could result in faster operation speed and thus larger modulation bandwidths. In addition, lattice-matched free-standing GaN substrates should provide superior heat dissipation and result in devices with lower threading dislocation densities compared to conventional sapphire substrates, allowing for operation at higher current densities where the modulation bandwidth can be maximized[12]. Thus, investigation of InGaN/GaN LEDs on free-standing nonpolar and semipolar GaN substrates is attractive for potentially improving high-speed operation [13,14].

In this project we intend to develop and evaluate the performance of high-speed LEDs on high-quality nonpolar $(10\bar{1}0)$ and semipolar $(20\bar{2}\bar{1})$ free-standing GaN substrates. In the previous report period, a systematic development of fast devices from mask layout design to fabrication and characterization of the devices were presented. Also, we developed an understanding of the underlying physics and recombination dynamics of high-speed LEDs (both optically and electrically-injected processes) which allows us to further design and implement more optimized structures for fast and efficient operations. In this report period, we demonstrate a significant improvement in the modulation bandwidth (up to a record 1.5 GHz) at low current densities using nonpolar LEDs. The low operation current density for GHz-class LEDs using nonpolar LEDs are crucial since it also minimizes the effect of efficiency droop and power consumption. In addition, we present a trade-off between modulation bandwidth and efficiency of LEDs required for dual illumination and communication applications. Furthermore, we demonstrate that using the carrier dynamics modelling we developed throughout the project, we were able to determine various parameters of LEDs, including injection efficiency, radiative efficiency, and their temperature dependence in actual operating conditions. Our understanding of nonpolar and semipolar high-speed LEDs can be used to further optimize designs for fast and efficient operation.

The content of the report is organized as follows. Section 2 presents an orientation dependence modulation response of InGaN/GaN LEDs. In section 3, our record modulation bandwidth of LEDs at low current densities using nonpolar LEDs will be presented. A discussion of the trade-off between bandwidth and efficiency for InGaN/GaN LEDs grown on a semipolar orientation will be discussed in section 4. Determination and evaluation of injection efficiency,

radiative efficiency, and the temperature-dependent recombination rates will be discussed in sections 5. The summary of achievements in the project will be presented in section 6, followed by future works in section 7.

2. Orientation-dependent frequency response of InGaN/GaN LEDs

High current densities (5-10 kA/cm^2) are typically needed to reduce the carrier lifetime and achieve a high modulation bandwidth with *c*-plane InGaN/GaN LEDs. However, high operating current densities are detrimental because of the resulting *efficiency droop*.[15–17] Thus, methods to reduce the current density for a given modulation bandwidth are of substantial interest since higher quantum efficiency could be achieved for a given bandwidth.

LEDs on nonpolar and semipolar orientations are potential candidates for achieving higher bandwidth at lower current density due to their larger electron-hole wavefunction overlaps and shorter carrier lifetimes.[10,11,18–21] In addition, particular semipolar orientations (e.g., semipolar $(20\bar{2}\bar{1})$) show very little efficiency droop, which was previously explained by a higher ratio of radiative to Auger recombination coefficients.[22] Nevertheless, there are no studies comparing the modulation responses for polar, nonpolar, and semipolar LEDs. Such studies would provide valuable information about which orientations are best suited to maximize speed at reasonably low current densities. In this work, the bandwidth *vs.* current density (J) characteristics for polar (0001), semipolar $(20\bar{2}\bar{1})$, and nonpolar $(10\bar{1}0)$ LEDs are experimentally compared for devices with a circular diameter of 60 μm. Clear trends are observed in the slopes (df_{3dB}/dJ) and y-intercepts of the modulation bandwidth *vs.* current density curves for the three orientations. The nonpolar and semipolar LEDs exhibit higher bandwidths at lower current densities, but lower (df_{3dB}/dJ) slopes at high current densities (where screening starts to occur), compared to the polar (0001) LEDs. The crystal schematics of the polar, semipolar, and nonpolar planes investigated in this study are shown in Fig. 2.1(a).

To show the trends in bandwidth *vs. J* as a function of orientation, we measured the modulation bandwidth as a function of current density for polar, semipolar, and nonpolar micro-LEDs. The InGaN/GaN LED samples each consist of three quantum wells with nominal thicknesses of 4 nm, 4 nm, and 6 nm for the polar, semipolar, and nonpolar structures,

respectively. The quantum well thicknesses were selected based on achieving the highest optical output power for each orientation with emission in the blue region (~450 nm). The semipolar and nonpolar structures were grown on freestanding GaN substrates from Mitsubishi Chemical Corporation (MCC) and the *c*-plane structure was grown on sapphire. Micro-LEDs having circular mesas with diameters of 60 μm were fabricated. Indium-tin oxide (ITO) was used as a *p*-contact, while Ti/Al/Ni/Au and Cr/Au were used as *n*-contacts and contact pads, respectively. The LEDs were designed with ground-signal-ground RF electrodes. Micro-LEDs were used to minimize the effects of the parasitic RC time constant on the evaluated modulation bandwidths.[7,9,20,23] More detailed descriptions of the growth and fabrication processes can be found elsewhere.[19,20]

The modulation responses of the LEDs were then evaluated using a micro-RF ground-signal-ground probe (ACP40-GSG-150, Cascade Microtech, Inc.) and network analyzer (NA) (Agilent PNA-X N5247A). The devices were biased with a DC voltage combined with a small-signal voltage (100 mV) and the emitted light was coupled to an optical fiber, which was connected to a high-speed photodetector (DET025AFC, ThorLabs, Inc.). The electrical signal was then amplified using a low-noise amplifier (LNA) (PE15A1009, Pasternack Enterprises) and received by the network analyzer. The frequency responses of the RF cables, bias tee, and low-noise amplifier were removed by calibration to reveal only the frequency response of the device. The frequency response of the optical signal was then evaluated for the 3dB modulation bandwidth (f_{3dB}). More details of the RF setup and measurements are described in Refs. [20,22–24].

Fig. 2.1(b) shows a comparison of the normalized S_{21} power for LEDs with polar, semipolar, and nonpolar orientation at an injected current density of 1 kA/cm^2. The nonpolar device exhibits the fastest frequency response, followed by the semipolar device, followed by the polar device. The extracted 3dB modulation bandwidths at 1 kA/cm^2 are 1050 MHz, 325 MHz, and 125 MHz for the nonpolar, semipolar, and polar LEDs, respectively. To better illustrate the comparison between the different orientations, Fig. 2.2 (a) shows the 3dB modulation bandwidth as a function of current density for the three orientations. Clear trends in the behavior of bandwidth *vs. J* are observed for the current density regime studied. The nonpolar LEDs have the highest bandwidth, followed by semipolar, followed by polar ($f_{3dB}(J)_{Nonpolar} > f_{3dB}(J)_{Semipolar} > f_{3dB}(J)_{Polar}$). The nonpolar LED shows a modulation bandwidth of ~1 GHz at low current

density of 500 A/cm^2. The major differences in bandwidth can be explained by the differences in the wavefunction overlap between the three orientations. For example, the square of the average wavefunction overlap in the nonpolar quantum wells is in the range of 3-8X higher than that of the *c*-plane quantum wells, depending on the current density.[21] Since both radiative and non-radiative recombination rates are known to scale with the square of the wavefunction overlap,[25,26] the speed is linked with the overlap through the carrier lifetime. As the current density increases, the coulomb screening effect[27] leads to a more significant change of band-bending in the polar LED, and the bandwidth increases at a faster rate with current density (note the larger slope of bandwidth *vs. J* above 500 A/cm^2 for the polar LED compared to the semipolar and nonpolar LEDs). Fig. 2.2 (b) shows the optical output power of the LEDs *vs.* current density as measured on-wafer into a photodetector. The output power of the semipolar device is more than two times that of the nonpolar device, whereas the output power of the polar device is slightly higher than the nonpolar device. We note that the bandwidth trends do not correlate one-to-one with the output power trends, suggesting a stronger effect from orientation than output power on speed.

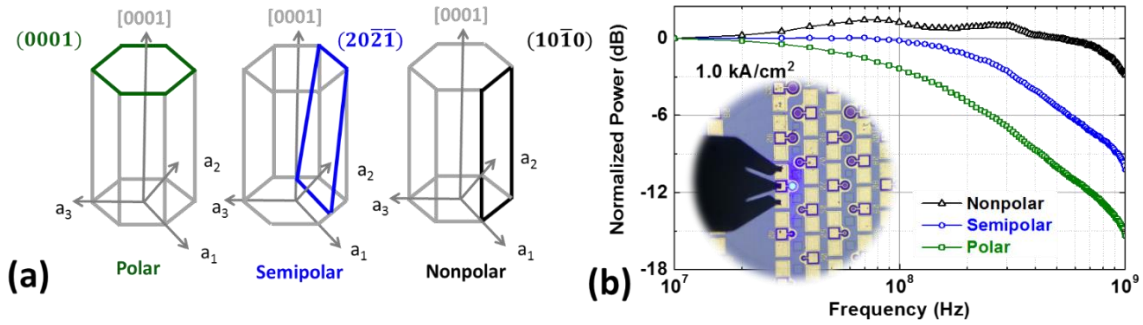

FIG. 2.1. (Color Online) (a) Schematic illustration of the crystallographic planes under study and (b) normalized S_{21} response of LEDs with polar (green squares), semipolar (blue circles), and nonpolar (black triangles) orientation with the same device geometry operating at 1 kA/cm^2. The inset of (b) shows an operating device probed using a GSG RF probe.

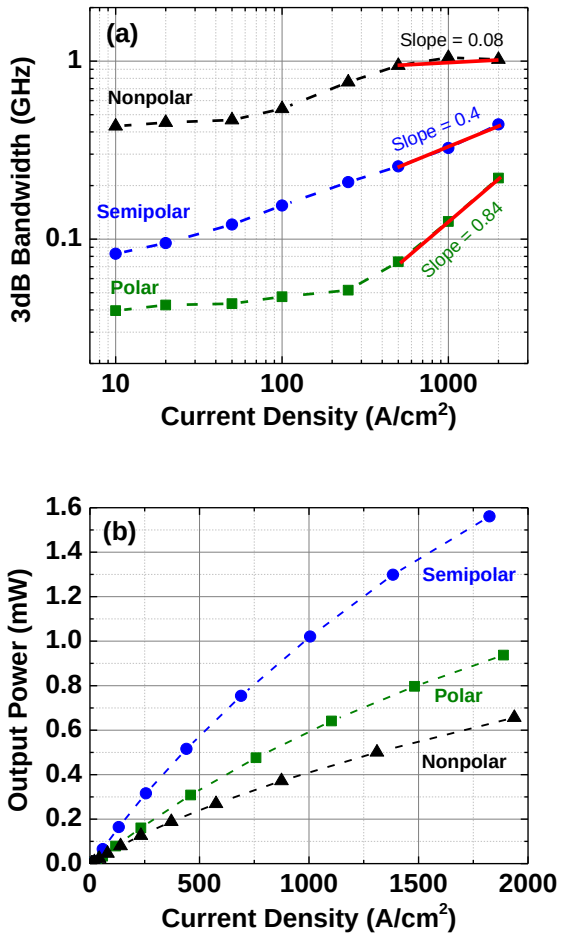

FIG. 2.2. (Color Online) (a) Bandwidth and (b) optical output power *vs.* current density for devices with polar (green squares), semipolar (blue circles), and nonpolar (black triangles) orientation. The dashed lines are guides to the eye.

After measuring the 3dB modulation bandwidths (f_{3dB}) as a function of current density for the three orientations (Fig 2.2 (a)), the differential carrier lifetimes (DLT) were obtained (Fig. 2.3(a)) for the given range of current densities using $\tau_{\Delta n} = 1/(2\pi f_{3dB})$, where $\tau_{\Delta n}$ is the DLT. We then calculated the corresponding injected carrier density for a given current density for each device, similar to the approach described in Refs. [22,28,29]

$$n = \int_0^G \tau_{\Delta n} dG \tag{2.1}$$

where n is the carrier density, and G is the generation rate, which is calculated from the current density (J), electron charge (e), and active region thickness (d) using $G = J/(e \times d)$.

The lower limit of the integral corresponds to a generation rate of zero, while the measurable minimum for the carrier lifetime corresponds to a non-zero generation rate, as previously discussed.[28] Extrapolating the data in Fig 2.3(a) to obtain the y-intercept, we extract the approximate Shockley-Read-Hall lifetimes (τ_{SRH}) for the three orientations at zero generation rate. The resulting SRH lifetime for nonpolar (0.4 ns) is shorter than that of semipolar (2.0 ns) and polar (4.0 ns). With the lower-limit lifetimes obtained, the carrier density is calculated. Figure 2.3(b) shows that the calculated carrier density is always lower in the case of nonpolar for a given current density, followed by semipolar, followed by polar ($n(J)_{polar} > n(J)_{semipolar} > n(J)_{nonpolar}$). This trend is explained by the higher recombination rates in nonpolar and semipolar, which relates back to the larger electron-hole wavefunction overlaps in nonpolar and semipolar.[14] A similar reduction in the recombination lifetime has also been achieved using external strain to increase the wavefunction overlap.[30] At high current densities, the DLT for the polar device decreases at a faster rate compared to the nonpolar and semipolar orientations due to coulomb screening of the polarization field. Hence, at very large current densities, the DLT of the polar device may potentially approach those of the nonpolar and semipolar devices. Indeed, *c*-plane LEDs have shown bandwidths near 1 GHz ($\tau_{\Delta n} \sim 0.16\, ns$) above ~5 kA/cm^2 (see Fig. 2.4). Table I compares the bandwidth, DLT, and carrier density for the different orientations at a current density of 1 kA/cm^2.

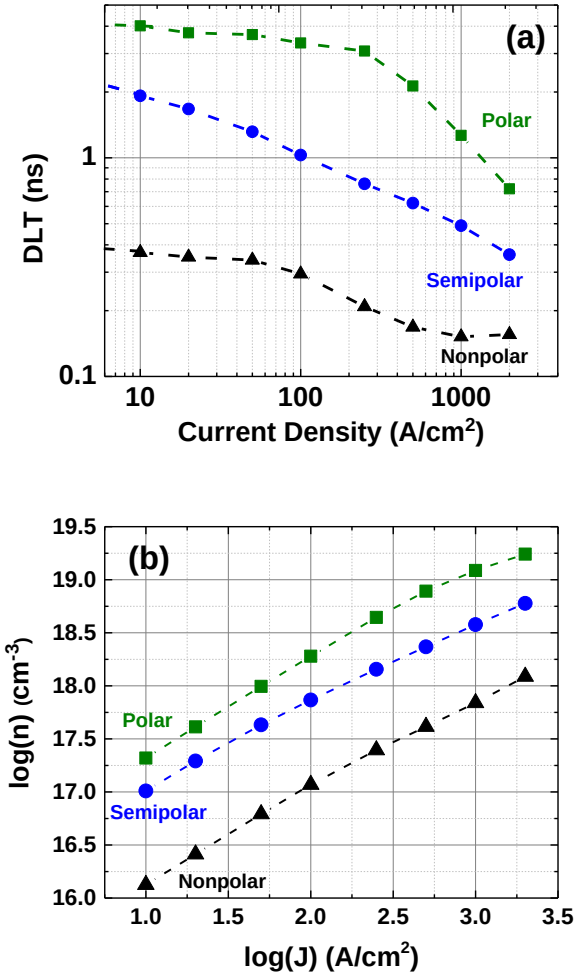

FIG. 2.3. (Color Online) (a) Differential carrier lifetime as a function of current density and (b) calculated log (n) *vs.* log (J) for LEDs with polar (green squares), semipolar (blue circles), and nonpolar (black triangles) orientation.

TABLE I. Comparison of bandwidth (BW), DLT, and carrier concentration at 1 kA/cm^2 for various orientations.

Orientation	*BW (MHz) / DLT (ns)*	*Carrier Conc. (cm^{-3})*
Nonpolar	1047 / 0.15	6.76×10^{17}
Semipolar	325 / 0.49	3.80×10^{18}
Polar	123 / 1.26	1.23×10^{19}

Fig. 2.4 compares the bandwidth *vs.* J trends for the LEDs from this study with several of the highest bandwidth *c*-plane LEDs, and semipolar $(11\bar{2}2)$ LEDs with 50 μm diameter,[31,32] that were previously reported. The bandwidth of the *c*-plane LED from this study is in excellent

alignment with the trends from previous studies, suggesting an intrinsic bandwidth limitation for *c*-plane LEDs (particularly at low current densities) regardless of the material structure and device design (e.g., standard *vs.* flip-chip). Conversely, the bandwidth of the nonpolar LED is significantly higher than those of the *c*-plane LEDs at low current densities where LEDs are more likely to operate efficiently due to reduced efficiency droop. Similar trends hold for the semipolar LEDs, although to a somewhat lesser degree. Thus, LEDs fabricated on nonpolar and semipolar orientations are attractive for achieving higher bandwidths at lower operating currents, which is advantageous for maximizing efficiency, reducing power dissipation, and mitigating issues with thermal management.

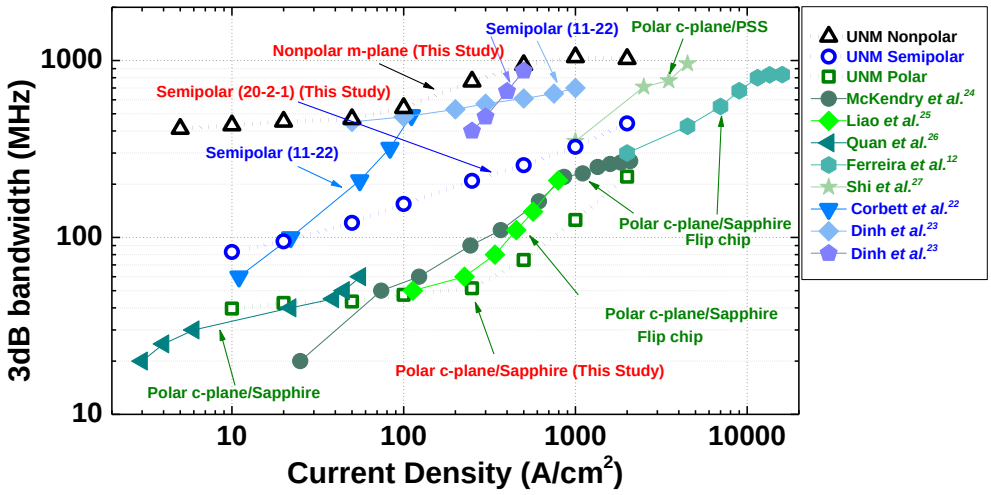

FIG. 2.4. (Color Online) Bandwidth *vs.* current density for the nonpolar LED (open black triangles), semipolar LED (open blue circles), and polar *c*-plane LED (open green squares) compared to other reported polar *c*-plane LEDs on sapphire or with a flip-chip design and compared to semipolar $(11\bar{2}2)$ LEDs. *c*-plane data from Refs. 6,7,33–35 and semipolar $(11\bar{2}2)$ data from Refs. 31,32.

In summary, the modulation bandwidth characteristics of polar (0001), semipolar $(20\bar{2}\bar{1})$, and nonpolar $(10\bar{1}0)$ InGaN/GaN LEDs were studied. The bandwidth of the nonpolar LEDs was the highest, followed by semipolar, followed by polar. This trend is consistent with the shorter carrier lifetimes expected in nonpolar and semipolar active regions due to the larger wavefunction overlaps. A 3dB modulation bandwidth ~1 GHz was obtained at a low current density of 500 A/cm^2 for the nonpolar LED, whereas the semipolar LED showed 260 MHz, and the *c*-plane LED showed 75 MHz. At large current densities, the bandwidth of the polar LED

may eventually approach that of the nonpolar and semipolar LEDs due to the coulomb screening effect. A comparison of the *c*-plane results from this study with *c*-plane results from other studies reveals an intrinsic limitation in the bandwidth of *c*-plane LEDs, particularly at low current densities. This trend is again explained in terms of the wavefunction overlap. The results show that nonpolar and semipolar LEDs exhibit larger modulation bandwidths at the relatively low current densities needed for LED operation where efficiency remains higher and power dissipation is lower. Such devices may be attractive as light sources in future VLC systems.

3. Nonpolar LED with record high 1.5 GHz bandwidth operating at low current densities

Last year, we reported a -3dB modulation bandwidth of 524 MHz from a nonpolar *m*-plane micro-LED with diameter of 60 µm. Initially in this project we were not able to exclude the effect of loss of the cables and electrical components in the RF setup from the measurements. This is due to the nature of the measurements where there are two signal conversions, first electrical-to-optical signal conversion by LED and second optical-to-electrical signal conversion by photodetector. Because of this the network analyzer (NA) is not able to perform a two-port calibration including the cables and electronic devices. This year we have adapted a technique where we remove the optical devices from the RF link and connect both ends of the link. We use a feature in the NA called *Response* to measure the loss in the link, save it, and subtract it from the subsequent measurements. More details of this procedure are presented in the following sections. Doing so, we were able to exclude the effect of the cables from the measurements and measured a record -3dB modulation bandwidth of 1.5 GHz at a current density of 1 kA/cm^2 for an 80-µm-diameter device on the nonpolar *m*-plane micro-LED sample. This is the highest bandwidth reported for any GaN-based LED to date. Moreover, the nonpolar micro-scale LED achieves a modulation bandwidth of 1.35 GHz at a current density of only 250 A/cm^2, which is attractive for minimizing power dissipation and efficiency droop. Using the full rate-equation model considering transport effects and carrier leakage which we developed last year, the differential carrier lifetime (DLT) at 1 kA/cm^2 is found to be 200 ps. The excellent high-speed performance is attributed to the large electron-hole wavefunction overlap and short carrier lifetime enabled by nonpolar quantum wells.

The LEDs were grown on a nonpolar $(10\bar{1}0)$ free-standing GaN substrate by metal organic chemical vapor deposition (MOCVD). The active region consists of three pairs of undoped InGaN (6 nm)/GaN (15 nm) quantum wells/barriers. The micro-LED consists of a circular mesa with a diameter of 80 μm, a transparent ITO *p*-contact, and RF electrodes, as shown in Figure 3.1 (a). The details of the growth and fabrication are reported in the report of year two. Figure 3.1 (b) shows the light-current density-voltage (L-J-V) characteristics of the device. A light output power >1.2 mW was collected on-wafer from the backside of the device at current density of 1 kA/cm^2. The peak wavelength *vs.* current density for this device ranges from 454 to 468 nm, as shown in Figure 3.1 (c). The inset of Figure 3.1 (c) shows the electroluminescence (EL) spectra of the LED at different current densities.

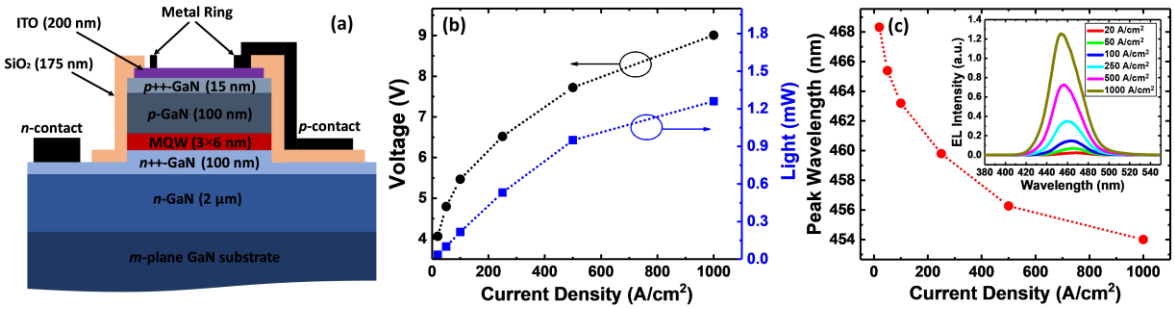

Figure 3.1 (a) High-speed nonpolar InGaN/GaN micro-LED. Layers not drawn to scale. (b) L-J-V characteristics of the high-speed LED. (c) Peak wavelength vs. current density. Inset: EL spectra at different current densities.

In our previous work (reported last year), the frequency responses of the RF cables, bias tee, and LNA were not calibrated out of the measurements. As a result, the speed of the previously reported LEDs was significantly limited by the bandwidth of the measurement system, which is ~650 MHz. In the present measurements, we removed the frequency response of all RF elements in the system, with the exception of the PD (1.7 GHz bandwidth) and the RF micro-probe (50 GHz bandwidth). To calibrate the RF link (cables, bias tee, LNA) using the NA, both ports of the link in Figure 3.2 (a) must be connected. Therefore, the PD, optical fiber, and RF probe were removed from the link during calibration to enable the connection of both ends. The NA calibration procedure measures the S_{21} of the RF link (cables, bias tee, and LNA), which is labeled as "RF link response" in Figure 3.1 (b), and automatically subtracts it from the LED frequency response. The response of the RF micro-probe is assumed to be flat over the frequency

range of interest. The response of the PD was measured using a high-speed laser (see Figure 3.1 (c)), but it is not subtracted in the calibration. Subtraction of the PD response would only further increase the measured LED bandwidth. To further clarify the effect of the link response on modulation bandwidth, the LED was biased at 1 kA/cm^2 and the frequency responses of the full link including the LED, RF probe, and PD were measured before and after applying the calibration and are shown as "LED without calibration" and "LED with calibration" in Figure 3.1 (b), respectively. Figure 3.1 (b) shows that the electrical -3dB bandwidth of the LED is limited by the RF link before the calibration. By calibrating out the RF link, the electrical -3dB bandwidth of the LED increases from ~650 MHz to ~1.5 GHz. The improved calibration techniques here give a more accurate measure of the inherent LED response.

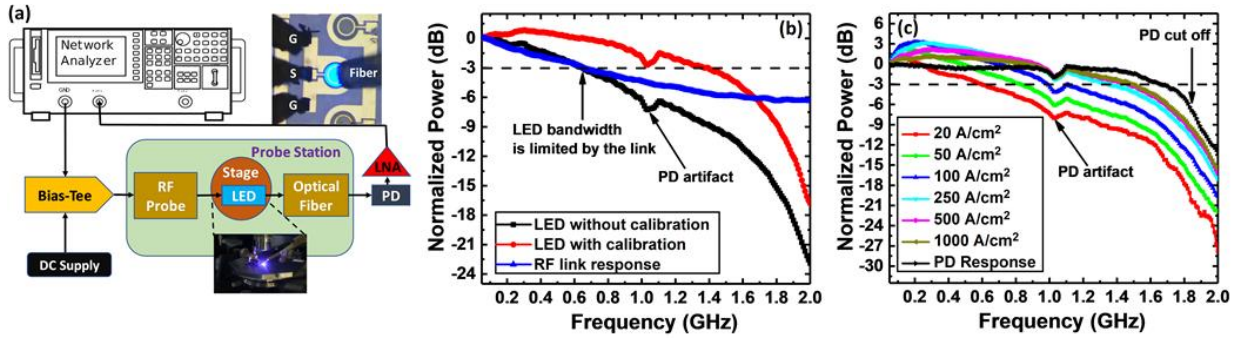

Figure 3.1 (a) The RF setup for measuring the frequency response of the LED. Top right: the device under RF GSG micro-probe. (b) Effect of calibration of the RF link on the frequency response of the LED. The response of the RF link is measured and plotted separately to show its effect on the modulation bandwidth of the LED. The responses of the full link, including the LED, measured before and after applying the calibration are also shown. (c) Frequency response of the nonpolar InGaN/GaN micro-LED at various current densities. The frequency response of the detector is also shown.

The normalized frequency response and electrical -3dB bandwidth of the LED vs. current density are shown in Figure 3.1 (c) and 3.3 (a), respectively. The electrical -3dB bandwidth of the LED varies from 601 MHz to 1.485 GHz at current densities ranging from 20 to 1000 A/cm^2. To best of our knowledge, this is the highest reported electrical -3dB bandwidth for an InGaN/GaN LED. Moreover, the LED achieves an electrical -3dB bandwidth of 1.35 GHz at a current density of only 250 A/cm^2. The large modulation bandwidth at low current density is enabled by the absence of internal electric fields. GaAs-based LEDs (which also lack internal electric fields) previously reached 1.7 GHz at ~250 A/cm^2 [36]. The PD frequency response is also included in Figure 3.1 (c) and was measured using a high-speed 450 nm InGaN/GaN laser biased

well above threshold. The PD response shows that the rapid high-frequency roll-over and the dip around 1 GHz in the LED's frequency response are artifacts from the PD response. The PD roll-over is partially responsible for the saturation of the LED electrical -3dB bandwidth in Figure 3.2 (a). The small rise in the frequency response of the LED below 100 MHz (Figure 3.1 (c)) is presumably a resonance behavior caused by small reflections of the RF signal. This behavior has been previously observed in both polar and semipolar InGaN/GaN micro-LEDs [37–41].

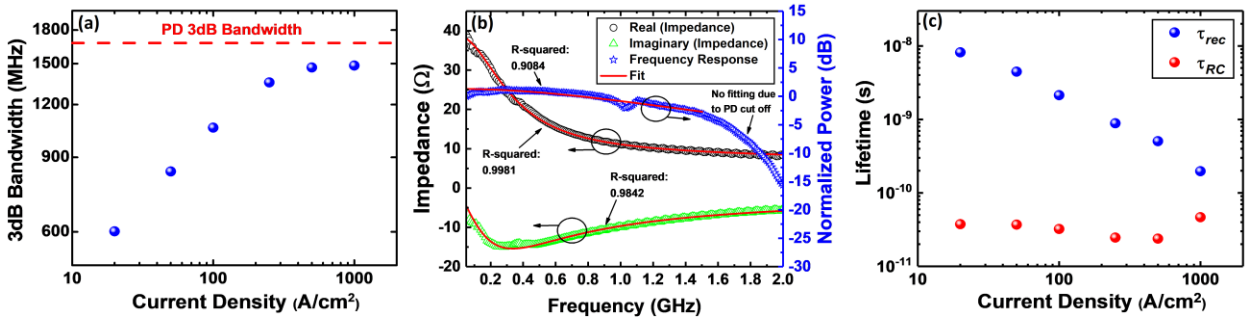

Figure 3.2 (a) Electrical -3dB bandwidth vs. current density for the LED. (b) Simultaneous fitting of impedance and frequency response of the small-signal circuit of [21] to the measured impedance and frequency response of the LED at a current density of 1 kA/cm^2. (c) Extracted DLT and RC time constant vs. current density.

To extract the DLT, our rate equation approach which we reported last year was used to derive the small-signal equivalent electrical circuit of the LED and simultaneously fit the impedance and frequency response of the circuit to the measured impedance and frequency responses of the LED [42]. Figure 3.2 (b) shows an example of the fitting for LED data at a current density of 1 kA/cm^2. Carrier transport in the cladding layers, recombination in the quantum wells, and escape from the quantum wells were considered in the model. Figure 3.2 (c) shows the extracted DLT (τ_{rec}), and RC time constant (τ_{RC}) at various current densities. The DLT and RC time constant range from 8 ns to 200 ps and 25 to 50 ps at current densities of 20 to 1000 A/cm^2, respectively. Although the RC time constant is negligible compared to the DLT at low current densities, they approach the same order of magnitude at higher current densities, resulting in a contribution from RC effects to the saturation of the electrical -3dB bandwidth in Figure 3.2 (a). The DLTs reported here for the nonpolar LED are smaller than those of *c*-plane LEDs operating at similar current densities [43–45].

In summary, we have demonstrated a nonpolar *m*-plane InGaN/GaN micro-scale LED with an electrical -3dB modulation bandwidth of 1.5 GHz at a current density of 1 kA/cm^2. The LED also exhibits an electrical -3dB bandwidth of 1.35 GHz at a current density of only 250 A/cm^2. The DLT was extracted at various current densities using a rate equation approach considering transport effects and carrier escape from the quantum wells. A DLT as short as 200 ps was obtained at a current density of 1 kA/cm^2. The high-speed and short DLT are attributed to the large electron-hole wavefunction overlap in polarization-free nonpolar InGaN/GaN quantum wells. The GHz bandwidth at low current densities pave the way for realization of multi Gb/s and low power VLC networks.

4. Trade-off between bandwidth and efficiency

As discussed, high-speed InGaN/GaN light-emitting diodes (LEDs) are of interest for visible-light communication (VLC) in emerging light-fidelity (Li-Fi) networks.[1,9] However, large modulation bandwidths are typically obtained at high current densities (10 to 15 kA/cm^2) where the internal quantum efficiency (IQE) is significantly degraded by *efficiency droop*. Intentional impurities have also induced a faster frequency response in GaAs-based LEDs due to the higher non-radiative recombination rate caused by the impurities.[46] Although increasing the non-radiative recombination may enhance the frequency response, the trade-off is lower IQE. Thus, it is critical to consider the IQE alongside the modulation characteristics to ensure both fast and efficient devices as required by lighting systems using VLC. Nevertheless, the majority of existing studies do not include an evaluation of the active layer quality via IQE measurements or absolute external quantum efficiency (EQE) measurements. We have previously shown that nonpolar and semipolar orientations of GaN with reduced polarization effects significantly increase the wavefunction overlap, decrease the carrier lifetime, and increase the modulation bandwidth at low current densities.[47] Obtaining high-speed at low current densities is essential to combat efficiency droop effects and simultaneously realize high modulation bandwidth and high IQE.[10,11,48] Several recent studies have investigated the small-signal modulation characteristics of hetero- or homo-epitaxially grown nonpolar and semipolar LEDs.[20,35,47,49,50]

Among semipolar and nonpolar orientations, LEDs grown on semipolar $(20\bar{2}\bar{1})$ have shown low efficiency droop, high brightness, large optical polarization, narrow emission linewidth, high

indium incorporation efficiency, and robust temperature stability.[22,51–56] Previously we demonstrated semipolar $(20\bar{2}\bar{1})$ LEDs with high peak IQEs.[19] In addition, semipolar $(20\bar{2}\bar{1})$ quantum-well (QW) LEDs exhibit a relatively flat QW profile at low bias since the direction of the polarization-related electric field is opposite to that of the built-in electric field in the *pn*-junction, which minimizes the net electric field. Thus, the wave function overlap is close to one at low bias and remains high for higher bias voltages.[53] The recombination rate in semipolar $(20\bar{2}\bar{1})$ LEDs was shown to be faster than that in *c*-plane LEDs.[47] The combination of high efficiency and high speed make the semipolar $(20\bar{2}\bar{1})$ platform attractive for studying the trade-offs between efficiency and speed in InGaN/GaN LEDs. So far, the highest efficiency LEDs on semipolar $(20\bar{2}\bar{1})$ used 12 to 14 nm-thick $In_{0.16}Ga_{0.84}N$/GaN single-quantum-well (SQW) structures.[52,57] However, no comparison of modulation characteristics between SQW and multiple-quantum well (MQW) designs (on any orientation) has been reported and the trade-offs between speed and efficiency have not been studied.

Here, we fabricate high-efficiency semipolar $(20\bar{2}\bar{1})$ LEDs with SQW and MQW active regions and compare their modulation characteristics. The LEDs were grown on free-standing GaN substrates and have peak emission wavelengths near 440 nm. The SQW active region consists of a 12-nm-thick $In_{0.15}Ga_{0.85}N$ SQW and has a peak IQE of 0.93. The MQW active region consists of three 4-nm-thick $In_{0.17}Ga_{0.83}N$ QWs separated by 4-nm-thick GaN barriers and has a peak IQE of 0.73. Both structures contain the same total QW thickness (12 nm). We demonstrate that although the peak IQE of the SQW LED is higher than the MQW LED by 27%, the MQW LED shows approximately 40-80% higher modulation bandwidth than the SQW LED and reaches 1.5 GHz at 13 kA/cm^2. We also evaluate the carrier recombination and escape lifetimes, which suggest that the MQW structure is faster at low current densities mainly due to faster Shockley-Read-Hall (SRH) or radiative recombination and faster at high current densities due to stronger coulomb-enhanced capture processes[23,58]. Finally, we compare the bandwidth and IQE characteristics of the two LED designs and introduce the bandwidth-IQE product as a potential figure of merit for optimizing speed and efficiency in InGaN/GaN LEDs.

The LEDs were grown on free-standing semipolar $(20\bar{2}\bar{1})$ substrates using atmospheric-pressure metal-organic chemical vapor deposition (MOCVD). The substrates have dislocation densities ~10^6 cm^{-2} and were obtained from Mitsubishi Chemical Corporation (MCC).

Trimethylgallium (TMG) and triethylgallium (TEG) were used as the Ga sources, while trimethylindium (TMI) was used as the In source. Bis(cyclopentadienyl)-magnesium (Cp_2Mg) and SiH_4 were used as the sources for Mg and Si dopants, respectively. First, a 2 μm-thick *n*-GaN layer was grown on the free-standing substrate with nominal Si concentration of 3×10^{18} cm^{-3}. Then, 12 nm of unintentionally doped GaN barrier was grown underneath the active regions. The active regions were later capped with a 10 nm *p*-$Al_{0.2}Ga_{0.8}N$ electron blocking layer (EBL) followed by a 100 nm *p*-GaN layer ([Mg] = 2×10^{19} cm^{-3}) and a 10 nm *p*++GaN layer ([Mg] = 1.6×10^{20} cm^{-3}). A more detailed description of the growth parameters can be found elsewhere.[19]

Micro-LEDs were then fabricated using an RF electrode design and semi-transparent indium-tin-oxide (ITO) *p*-contacts to improve the light extraction efficiency. First, 200 nm of ITO was blanket deposited on both structures using electron-beam evaporation. Circular mesa structures with 60 μm diameter were then formed by etching the ITO and epitaxial layers using inductively coupled plasma (ICP) etching and the ITO was annealed in N_2 at 550 ^{0}C for 10 minutes in a rapid thermal annealer (RTA). 200 nm of SiO_2 was then conformally deposited using electron-beam evaporation to isolate the *p*- and *n*-regions of the devices. Finally, Ti/Al/Ni/Au (20/100/50/600 nm) and Cr/Au (20/750 nm) were deposited as the *n*-contact and *p*-pad, respectively. Figure 4.1 (a) shows a cross-sectional schematic of the fabricated devices. An image of a micro-LED biased using a ground-signal-ground (GSG) RF probe at a current density of 20 A/cm^2 is shown in Figure 4.1 (b). Figure 4.1 (c) shows the electroluminescence (EL) spectra of both LEDs at a current density of 1 kA/cm^2. The five nanometer difference in peak wavelength is not expected to significantly affect the IQE or the bandwidth since this corresponds to only 0.02 difference in indium composition.

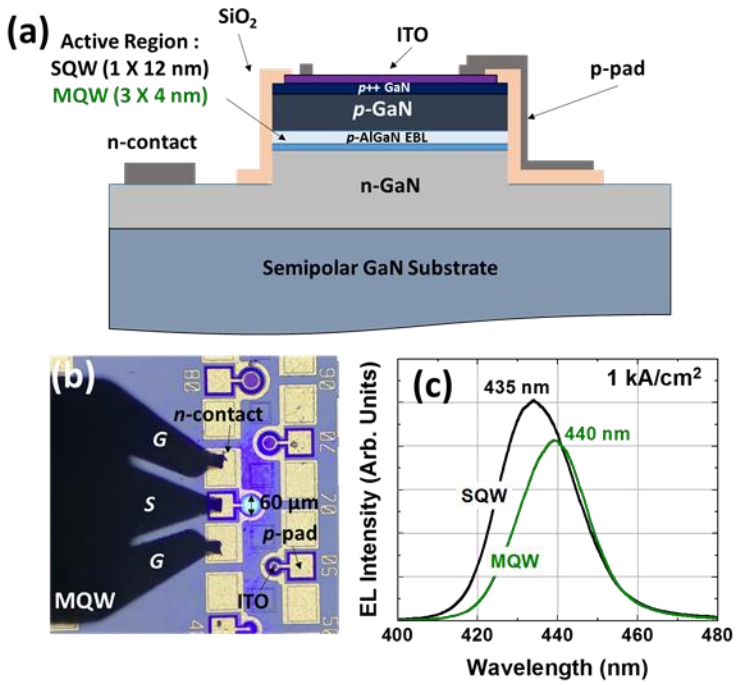

Figure 4.1. (a) Cross-sectional schematic of the fabricated semipolar $(20\bar{2}\bar{1})$ LEDs with SQW and MQW designs on free-standing substrates. (b) Plan-view optical microscopic image of a working device probed using a ground-signal-ground (GSG) RF probe. (c) EL spectra of the SQW and MQW devices at 1 kA/cm^2.

Figure 4.2 (a) shows the modulation bandwidths of the semipolar SQW and MQW LEDs with aperture diameter of 60 µm for selected injection current densities of 0.1 kA/cm^2, 1.0 kA/cm^2, and 5.0 kA/cm^2. The modulation bandwidth increases with current injection as expected from the reduction in differential carrier lifetime (DLT).[7,20] Figure 4.2 (b) shows the electrical -3 dB modulation bandwidth and reveals that the MQW LED is faster than the SQW LED by 40 to 80% over the full range of current densities (20 A/cm^2 to 13 kA/cm^2). The higher speed of the MQW LED is consistent with the shorter recombination lifetime for the MQW LED previously revealed using time-resolved photoluminescence (TRPL).[19]

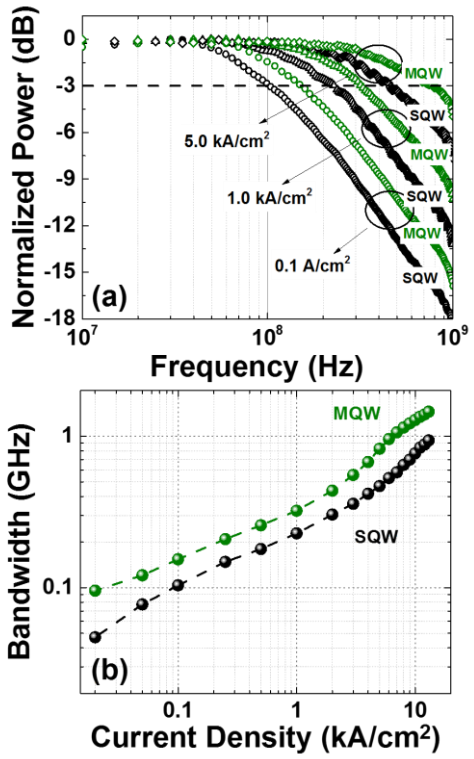

Figure 4.2. (Color Online) (a) Frequency response for selected current densities of 0.1, 1.0, and 5.0 kA/cm^2 and (b) -3 dB modulation bandwidth as a function of current density from 20 A/cm^2 to 13 kA/cm^2 for $(20\bar{2}\bar{1})$ SQW and MQW LEDs.

The frequency response (S_{21}) and input impedance (Z_{11}) of the devices were then simultaneously fit using a rate equation-based recombination model described earlier[23] to obtain the DLT (τ_{rec}), RC lifetime (τ_{RC}), and net carrier escape lifetime (τ_{esc}) as a function of current density. Figure 4.3 (a) shows the extracted DLT and RC lifetimes *vs.* current density, while Figure 4.3 (b) shows the extracted net escape lifetime *vs.* current density. The DLT reduces with current density reaching the RC lifetime at high current densities. The RC lifetimes for both devices are similar at the same current densities due to the similar epitaxial layer structures and same device layout for both LEDs. However, the DLT is shorter for the MQW LED at all current densities as expected from the bandwidth results of Figure 4.2 (b) and from previous PL lifetime measurements[19]. At low current densities, the DLT for the MQW LED is shorter than that of the SQW LED, which may be related to the shorter SRH recombination lifetime, higher carrier injection non-uniformity,[59] and/or larger wavefunction overlap in the thinner QWs in the MQW LED. At high current densities (> 3 kA/cm^2), the contribution of the RC lifetime to the

bandwidth becomes comparable to the DLT. However, the total bandwidth still increases due to the fast reduction of DLT at high current densities, which we attribute to a coulomb-enhanced capture process that rapidly increases the recombination rate in the QWs[58]. We note that the rapid decrease in carrier lifetime is not attributed to Auger recombination because the onset of Auger recombination (efficiency droop) occurs at much lower current densities (~100-200 A/cm^2) in these LEDs, as shown in Figure 4.4 (a). Furthermore, the Auger process does not appear to be significantly faster than the SRH or radiative processes since the DLT *vs.* current density curves have relatively constant slope below the onset of coulomb-enhanced capture. The coulomb-enhanced capture process (τ_{cou}) occurs at high current densities when the populations of carriers in the cladding layer and unconfined carriers above the QW are large and an unconfined carrier more easily scatters to the QW due to the coulombic repulsion between carriers above the QW and carriers in the cladding layer. This carrier scattering process opposes carrier leakage (τ_{leak}) from the QW, resulting in a higher population of carriers in the QW[23,58] and a corresponding reduction of the DLT. Figure 4.3 (b) shows the net escape lifetime (τ_{esc}) *vs.* current density. Closed data points represent the regime where the net escape rate is dominated by carrier leakage, while open data points represent current densities where the net escape rate is negative and dominated by coulomb-enhanced capture. Figure 4.3 (b) shows that the net escape time is similar for the SQW and MQW LEDs at low current densities. At high current densities, the coulomb-enhanced capture process is faster for the MQW LED, which leads to an increase in the carrier density in the QWs, resulting in the fast reduction in DLT for the MQW LED in Figure 4.3 (a). The onset of coulomb-enhanced capture at ~2 kA/cm^2 is consistent with the increase in slope for the MQW LED in Figure 4.2 (b). The shorter DLT results in a sort of carrier clamping in the QWs at high current densities.[60] The rate of coulomb-enhanced capture is greater in the MQW LED due to the thinner QWs, which result in a larger density of unbound carriers above the QWs. The coulomb-enhanced capture lifetime is inversely proportional to the number of carriers in the cladding.[58] Therefore, the smaller τ_{cou} for the MQW LED in Fig. 4.3(b) implies a larger number of carriers in the cladding of the MQW LED compared to the SQW LED. The increase in τ_{RC} above 2 kA/cm^2 for the MQW LED in Fig. 4.3(a) is related to the larger number of carriers in the cladding, which causes the capacitance to rise. The increase in τ_{RC} occurs at a similar current density to the onset of coulomb-enhanced capture. A similar increase in τ_{RC}

begins to manifest for the SQW LED, but it is less prominent since there are fewer carriers in the cladding.

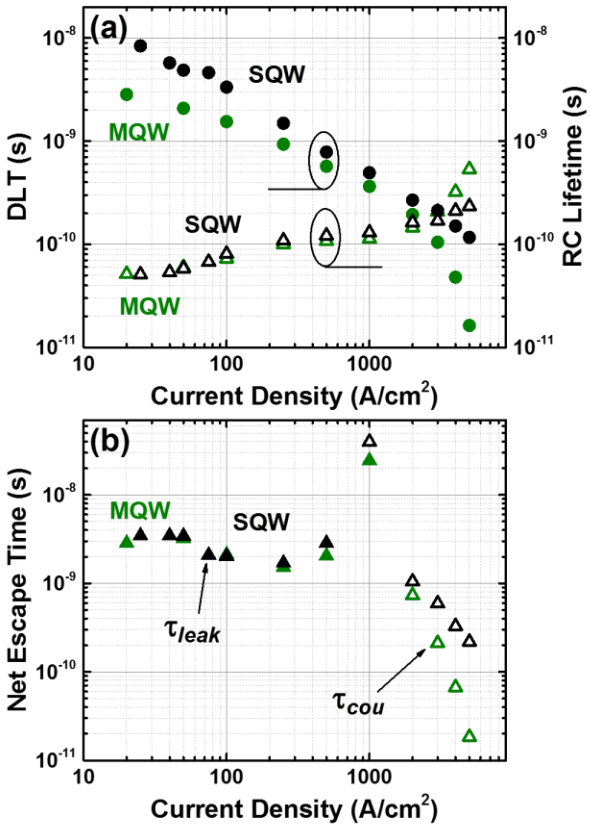

Figure 4.3. (Color Online) (a) DLT, RC lifetimes, and (b) net escape lifetimes as a function of current density as extracted from simultaneous fitting of S_{21} and Z_{11} using a rate equation-based modeling for $(20\bar{2}\bar{1})$ SQW and MQW LEDs on free-standing substrates.

Although bandwidths up to 1.5 GHz are achievable above 10 kA/cm^2, the greater interest is in bandwidths at lower current densities where one can minimize the effect of *efficiency droop* and reduce the device power consumption for VLC applications. Here, we consider the trade-off between bandwidth and IQE in the SQW and MQW LEDs. To estimate the IQE, we used relative EQE to determine the shape of the IQE *vs.* current density curve under continuous wave (CW) operation. The peak IQE value was estimated from previous optical measurements[19] based on comparing the room-temperature (295 K) and low-temperature (10 K) integrated photoluminescence (PL). The peak IQEs are 0.73 and 0.93 for the MQW and SQW LEDs, respectively. Figure 4.4 (a) shows the bandwidth and IQE *vs.* current density curves for the LEDs

under CW operation. Above ~ 100-200 A/cm^2, the IQE reduces (due to efficiency droop and heating) while the bandwidth increases with current density. The SQW LED shows higher IQE (except at very low current densities) and lower bandwidth than the MQW LED. Based on the trade-off between bandwidth and efficiency, we consider a bandwidth-efficiency figure of merit (BEFOM) to be the product of the bandwidth and IQE at a given current density ($BEFOM(J) = f_{3dB}(J) \times IQE\ (J)$). Figure 4.4 (b) compares the BEFOM for the two designs. The MQW LED shows an overall higher BEFOM than the SQW LED at low and high current densities ($J < 200A/cm^2$ and $2kA/cm^2 < J$) and a similar BEFOM at intermediate current densities ($200A/cm^2 < J < 2kA/cm^2$). The differences in the BEFOM for the SQW and MQW LEDs result from the individual bandwidth and IQE characteristics. For example, at low current densities, the significantly shorter SRH lifetime for the MQW LED (obtained by extrapolating the DLT to zero current density[22,28] in Fig. 4.3 (a)) is responsible for the higher bandwidth and an overall larger BEFOM. Additional effects such as carrier injection non-uniformity and wavefunction overlap may be secondary contributors to the differences in the modulation bandwidths of SQW and MQW LEDs at low current densities. At high current densities (> 2 kA/cm^2), the higher rate of coulomb-enhanced capture in the MQW LED results in a larger bandwidth, again leading to a higher BEFOM. Furthermore, the onset of efficiency droop (~100-200 A/cm^2) does not significantly alter the BEFOM *vs.* current density as indicated by similar values of BEFOM for the SQW and MQW LEDs up to onset of coulomb-enhanced capture (~ 2 kA/cm^2). Finally, we plot IQE as a function of bandwidth for the two designs as shown in Figure 4 (c). As expected, IQE drops as bandwidth increases due to efficiency droop and heating. As a result, larger modulation bandwidths can be obtained at the expense of lower IQE in InGaN/GaN LEDs.

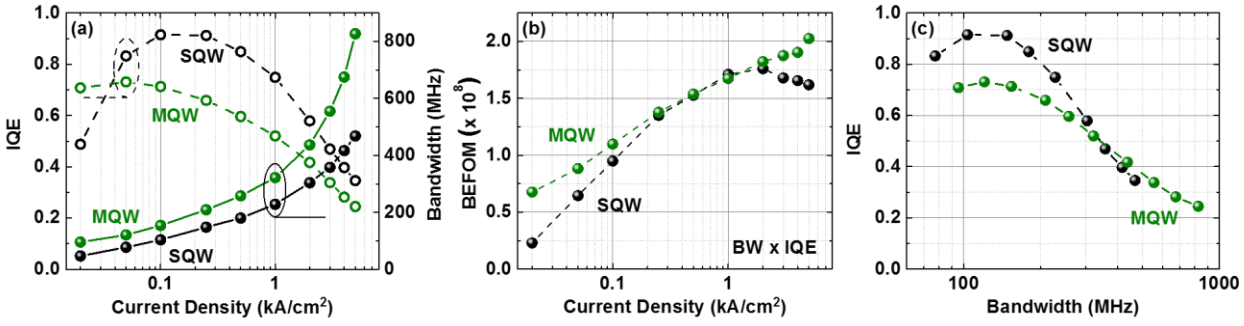

Figure 4.4. (Color Online) (a) IQE and bandwidth *vs.* current density, (b) BEFOM *vs.* current density, and (c) IQE *vs.* bandwidth for SQW (black symbols) and MQW (green symbols) LEDs.

In summary, we compared the modulation characteristics of high-efficiency SQW and MQW semipolar $(20\bar{2}\bar{1})$ LEDs with the same total active region volume and peak IQEs of 0.93 and 0.73, respectively. Although the peak IQE of the SQW LED is higher than that of the MQW LED by 27%, the MQW LED showed approximately 40-80% higher modulation bandwidth than the SQW LED and reached 1.5 GHz at 13 kA/cm^2. The carrier recombination and escape lifetimes were evaluated and suggest that the MQW structure is faster at low current densities due to faster SRH or radiative recombination and faster at high current densities due to a rapid drop in the DLT caused by stronger coulomb-enhanced capture processes. The results also show that Auger recombination does not play a dominant role in the speed at high current densities. Lastly, we investigated the trade-offs between bandwidth and efficiency and introduced the bandwidth-IQE product as a potential figure of merit for optimizing speed and efficiency in InGaN/GaN LEDs.

5. Rate-equation based recombination modeling

VLC systems are required to simultaneously provide illumination and data communication. Therefore, co-optimization of efficiency and modulation bandwidth is vital in realization of Gb/s low power consuming VLC networks. However, this critical topic has not been touched so far. We developed a rate equation-based measurement method last year to extract differential carrier lifetime and RC time constants of the LEDs. This allowed us to understand the limiting factors in the bandwidth of the LEDs. However, with some improvement of this method this year we were able to study efficiency droop in nitride LEDs. Efficiency droop reduces the efficiency of nitride LEDs with increasing current density. Despite two decades of studies of efficiency droop, its origin is still a controversy. Here, we use our unique method to study carrier dynamics of the LEDs to investigate different elements of efficiency of the LEDs in search of an answer to this long-debated topic. First, we measure the injection efficiency of the LEDs under electrical injection and show that the injection-related mechanisms are not the cause of efficiency droop. Then, we develop a pulsed-RF measurement technique to enable measurement of RF characteristics and study of carrier dynamics under isothermal conditions. The pulsed-RF technique allows us to characterize semiconductor devices on chip by excluding the thermal

effects. Using this technique, we were able to study origin of efficiency and thermal droop. This section starts with the measurement of injection efficiency and followed by the study droop.

5.1. Exclusion of injection efficiency as the primary cause of efficiency droop in InGaN/GaN LEDs

InGaN/GaN LEDs are ubiquitous in solid-state lighting and attractive for future micro-pixel displays and visible-light communication (VLC) [61]. Although InGaN/GaN LEDs exhibit a high peak internal quantum efficiency (IQE) at low current densities, efficiency droop reduces the IQE at high current densities [62]. Previous explanations for efficiency droop are divided into two primary categories: (1) reduction of the radiative efficiency due to Auger recombination[63–65], defect-assisted recombination [66], or saturation of the radiative rate[67] and (2) poor electrical injection efficiency due to carrier leakage from the active region[68,69] or ballistic carriers overshooting the active region [70,71]. Structures containing electron blocking layers (EBLs) [72], staircase electron injectors (SEIs) [71], and wide QWs [73] have been investigated for reducing electron leakage and overshoot. However, LEDs containing these structures still exhibit efficiency droop, suggesting that injection-related mechanisms are not the sole cause of efficiency droop. Previous investigations of carrier leakage employed resonant optical pumping of the QWs and measured the photocurrent [69,74]. With optical pumping, photogenerated carriers are directly injected into the QWs, failing to capture the effects of carrier transport under electrical injection and the subsequent interaction between carriers in the QWs and cladding. Recently, measurements of the escape lifetime under electrical injection have shown that carrier transport in the cladding layers strongly affects the carrier leakage process [42,75]. Thus, investigation of injection efficiency under electrical injection is necessary to fully understand its potential contribution to efficiency droop.

In this section, we extract the injection efficiency as a function of current density in SQW semipolar $(20\bar{2}\bar{1})$ InGaN/GaN LEDs using small-signal RF measurements and rate equation analysis of the dominant carrier mechanisms[42]. The rate equations are used to derive a small-signal equivalent circuit that yields expressions for the modulation response and input impedance of the LED. Simultaneous fitting of the modulation response and input impedance of the circuit

to the measured modulation response and input impedance of the LED gives the DLT, net differential carrier escape time from the active region, and differential recombination lifetime in the cladding layers. The extracted differential lifetimes are used to calculate the injection efficiency of the LED at various current densities. The injection efficiency increases with current density, reaching almost one at high current densities and indicating that injection-related mechanisms (e.g., carrier leakage and/or ballistic overshoot) are not the primary cause of efficiency droop in semipolar $(20\bar{2}\bar{1})$ LEDs.

The SQW LED was grown on a semipolar $(20\bar{2}\bar{1})$ free-standing GaN substrate using metal organic chemical vapor deposition (MOCVD). The growth and fabrication details are reported elsewhere [76,77]. The LED structure consists of a 2-µm-thick *n*-GaN, 12-nm-thick unintentionally doped (UID) GaN barrier, 12-nm-thick $In_{0.15}Ga_{0.85}N$ SQW, 12-nm-thick UID GaN barrier, 10-nm-thick *p*-$Al_{0.20}Ga_{0.80}N$ EBL, 100-nm-thick *p*-GaN, and 10-nm-thick *p*++-GaN contact layer. A 200-nm-thick ITO layer was deposited as a transparent *p*-contact and inductively coupled plasma (ICP) etching was used to fabricate circular mesas structures on the sample. The device reported here has a 50-µm-diameter mesa.

To formulate the carrier rate equations, we first consider the energy band diagram of the LED. Figure 1 (a) shows a schematic of the energy band diagram of the LED and the dominant carrier processes in the QW and cladding layers under flat-band conditions. N_w and N_c are the carrier numbers in the QW and cladding layers, respectively. V_w and V_c are the quasi-fermi level separation in the QW and cladding layers, respectively. I is the injected current into the cladding layers and $C_{sc}\frac{dV_c}{dt}$ is the current required to charge the space charge capacitance (C_{sc}) of the junction. $\tau_c = \tau_{cap} + \tau_{diff}$ is the delay that the carriers (N_c) experience in the cladding layer after they diffuse towards (τ_{diff}) and are captured by the QW (τ_{cap}). Carriers in the QW (N_w) either escape the QW (τ_{esc}) or recombine in the QW (τ_{rec}). The escaped carriers can either recombine in the cladding layers ($\tau_{rec,clad}$) or be re-captured by the QW. The net escape rate is altered by an interband carrier-carrier scattering process known as Coulomb-enhanced capture, where an unconfined carrier is captured into the QW due to scattering with an unconfined carrier in the cladding triggered by a Coulomb force.[15] Since Coulomb-enhanced capture opposes carrier leakage, the net escape time (τ_{esc}) is defined as $\frac{1}{\tau_{esc}} = \frac{1}{\tau_{leak}} - \frac{1}{\tau_{cou}}$, where τ_{leak} and τ_{cou}

are the carrier leakage and Coulomb-enhanced capture times, respectively. Carrier leakage includes thermionic emission of carriers from the QW and carrier overflow. The carriers that are ballistically transported to the other side of the QW either recombine as minority carriers (and the effect is folded into $\tau_{rec,clad}$) or are captured by the QW. Therefore, the effect of ballistically transported carriers is accounted for by $\tau_{rec,clad}$ and τ_{cap}. Figure 5.1 (b) summarizes the carrier dynamics in the QW. Any effects of crystal orientation and polarization-related electric fields are folded into the various lifetimes. For example, τ_{rec} for a semipolar QW will be shorter than τ_{rec} for a *c*-plane QW at a given current density due to the larger electron-hole wavefunction overlap in semipolar [78]. Moreover, we consider single-particle rate equations, assuming electrons dominate the carrier dynamics (i.e., hole leakage is small and hole transport between QWs is not an issue in SQW LEDs). Previously, our group and others showed that this single-particle model accurately describes the electrical characteristics of LEDs [42,45,79]. The single-particle rate equations governing the mechanisms in the active and cladding layers are written as follows:

$$\frac{dN_w}{dt} = \frac{N_c}{\tau_c} - \frac{N_w}{\tau_{rec}} - \frac{N_w}{\tau_{esc}} \tag{5.1}$$

$$\frac{dN_c}{dt} = \frac{I}{q} - \frac{C_{sc}}{q}\frac{dV_c}{dt} - \frac{N_c}{\tau_c} + \frac{N_w}{\tau_{esc}} - \frac{N_c}{\tau_{rec,clad}} \tag{5.2}$$

where q is the electron charge. The differential forms of Eqs. (5.1) and (5.2) are shown in Eqs. (5.3) and (5.4), respectively,[21] and can be used to derive the equivalent small-signal electrical circuit for the LED, which is shown in Figure (c).

$$\frac{d}{dt}(dN_w) = \frac{dN_c}{\tau_{\Delta c}} - \frac{dN_w}{\tau_{\Delta rec}} - \frac{dN_w}{\tau_{\Delta esc}} \tag{5.3}$$

$$\frac{d}{dt}(dN_c) = \frac{dI}{q} - \frac{\mathrm{C}_{sc}}{q}\frac{d}{dt}(dV_c) - \frac{dN_c}{\tau_{\Delta c}} + \frac{dN_w}{\tau_{\Delta esc}} - \frac{dN_c}{\tau_{\Delta rec,clad}} \tag{5.4}$$

where the differential quantities are of the small-signal form (e.g., $dI = ie^{j\omega t}$) and the lifetimes are differential lifetimes (e.g., $\tau_{\Delta rec}$ instead of τ_{rec}). The detailed derivation of this circuit is similar to that in Ref. 8. Here, $\tau_{\Delta rec,clad} = R_{rec,clad}C_c$ is defined using the same analogy as $\tau_{\Delta \mathrm{c}} = R_c C_c$ and $\tau_{\Delta \mathrm{rec}} = R_w C_w$ in Ref. 8. R_c and C_c are associated with the resistance and

capacitance due to the differential carriers in the cladding layers. $R_{rec,clad}$ is the resistance associated with the number of differential carriers that recombine in the cladding layers. The same analogy is applied to R_w and C_w, which are associated with the differential confined carriers in the QW.

The injection efficiency can be found considering the rate equations (5.1) and (5.2) in steady state, where $\frac{dN_w}{dt} = \frac{dN_c}{dt} = \frac{dV_c}{dt} = 0$. The injection efficiency is the current associated with recombination in the quantum wells ($I_w = \frac{qN_w}{\tau_{rec}}$) divided by the total current injected into the device. Therefore the injection efficiency (η_{inj}) is given by:[22]

$$\eta_{inj} = \frac{I_W}{I} = \frac{\frac{qN_w}{\tau_{rec}}}{I} = \frac{1}{1 + \frac{\tau_c}{\tau_{rec,clad}}\left(1 + \frac{\tau_{rec}}{\tau_{esc}}\right)} \tag{5.5}$$

However, since here we use small-signal measurements that yield the differential lifetimes rather than the total lifetimes, the differential rate equations (5.3) and (5.4) must be used instead to find the injection efficiency. By direct analogy to Eq. (5.5), Eqs. (5.3) and (5.4) under steady state and the circuit parameters in Figure 3.1 (c) yield the differential injection efficiency ($\eta_{\Delta inj}$)

$$\eta_{\Delta inj} = \frac{dI_w}{dI} = \frac{q\frac{dN_w}{\tau_{\Delta rec}}}{dI} = \frac{1}{1 + \frac{\tau_{\Delta c}}{\tau_{\Delta rec,clad}}(1 + \frac{\tau_{\Delta rec}}{\tau_{\Delta esc}})} = \frac{1}{1 + \frac{R_c}{R_{rec,clad}}\left(1 + \frac{\tau_{\Delta rec}}{\tau_{\Delta esc}}\right)} \tag{5.6}$$

where $dI_w = q\frac{dN_w}{\tau_{\Delta rec}}$ is the differential recombination current in the QW. The injection efficiency is then found by integration using the differential injection efficiency

$$\eta_{inj} = \frac{I_w}{I} = \frac{\int_0^I \eta_{\Delta inj} dI}{I} \tag{5.7}$$

To solve the numerical integral in Eq. (5.7), the differential injection efficiency at zero current is required, while technically the carrier lifetimes can only be measured down to some minimum bias current (i.e., sufficient light is required to measure the modulation bandwidth). Thus, we linearly extrapolate from the values of differential carrier lifetimes at low current to zero current to estimate the differential injection efficiency at zero bias [80]. The differential injection efficiency

represents the response to a small signal added to a DC bias and is the local slope of the recombination current in the QW vs. the injected current (dI_w/dI).

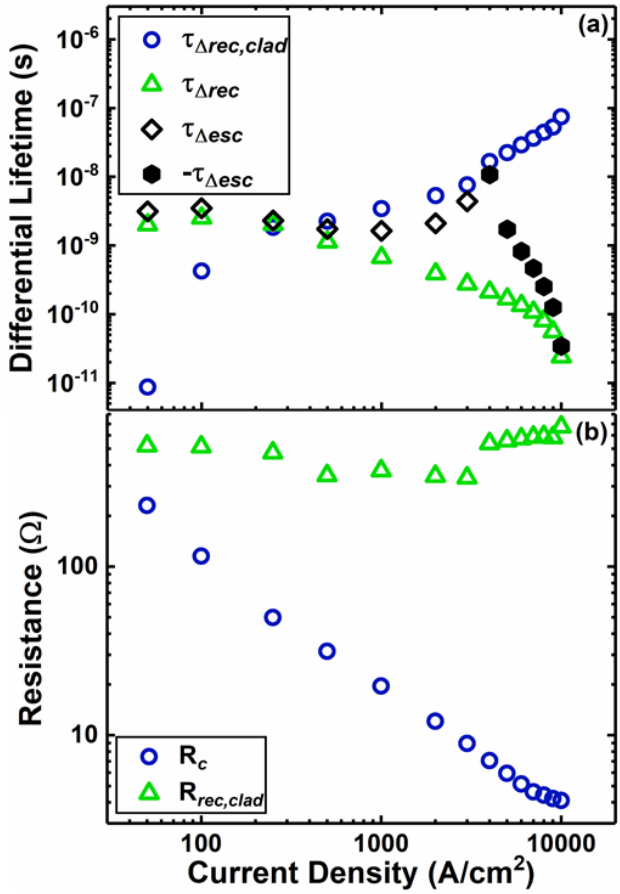

Figure 5.1 (a) Dominant carrier processes in the QW and cladding layers, (b) Coulomb-enhanced capture process opposing carrier leakage, and (c) small-signal equivalent electrical circuit of the LED.

The modulation response and input impedance of the LED were measured using a network analyzer by combining a time-dependent small-signal voltage with peak amplitude ~100 mV to the DC bias of the LED. To determine the injection efficiency, the parameters of the circuit in Fig. 1(c) were extracted by simultaneously fitting the modulation response ($H(\omega) = \frac{v_{out}(\omega)}{v_{in}(\omega)}$) and input impedance ($Z_{in}(\omega) = \frac{v_{in}(\omega)}{i(\omega)}$) of the circuit to the measured modulation response and input impedance of the LED for a frequency range of 10 MHz to 2 GHz [42]. Excellent fittings with R-squared values above 0.95 were achieved. Figure 5.25.2 (a) shows the DLT ($\tau_{\Delta rec}$), absolute value of the net differential escape time ($\tau_{\Delta esc}$), and differential

recombination lifetime in the cladding ($\tau_{\Delta rec,clad}$) at various current densities. The DLT ($\tau_{\Delta rec}$) reduces with increasing current density due to a faster recombination rate in the QW [81]. The net differential escape time slightly reduces with increasing current density at low injection levels, but increases at higher injection levels and eventually becomes negative around 4 kA/cm^2. The initial reduction of the differential escape time ($\tau_{\Delta esc}$) was previously attributed to the leakage of carriers from the active region into the cladding increasing the escape rate ($\tau_{\Delta cou} > \tau_{\Delta leak}$) [82]. With higher injection, the population of unconfined carriers in the cladding layer increases, resulting in Coulomb-enhanced capture that causes the net escape rate to reduce and eventually become negative ($\tau_{\Delta leak} > \tau_{\Delta cou}$) [45]. Later we calculate the total carrier numbers in the QW and cladding layers and show that the onset of the negative escape time is where the number of unconfined carriers in the cladding becomes comparable to the number of the confined carriers in the QW. The differential recombination lifetime in the cladding layers ($\tau_{\Delta rec,clad}$) increases with current density. As minority electrons build up in the UID cladding between the QW and EBL (where a high hole population exists from the EBL doping and hole injection from the *p*-side), some holes are lost through recombination with the minority electrons, making fewer holes available for subsequent electrons to recombine with, increasing the electron lifetime in the cladding.

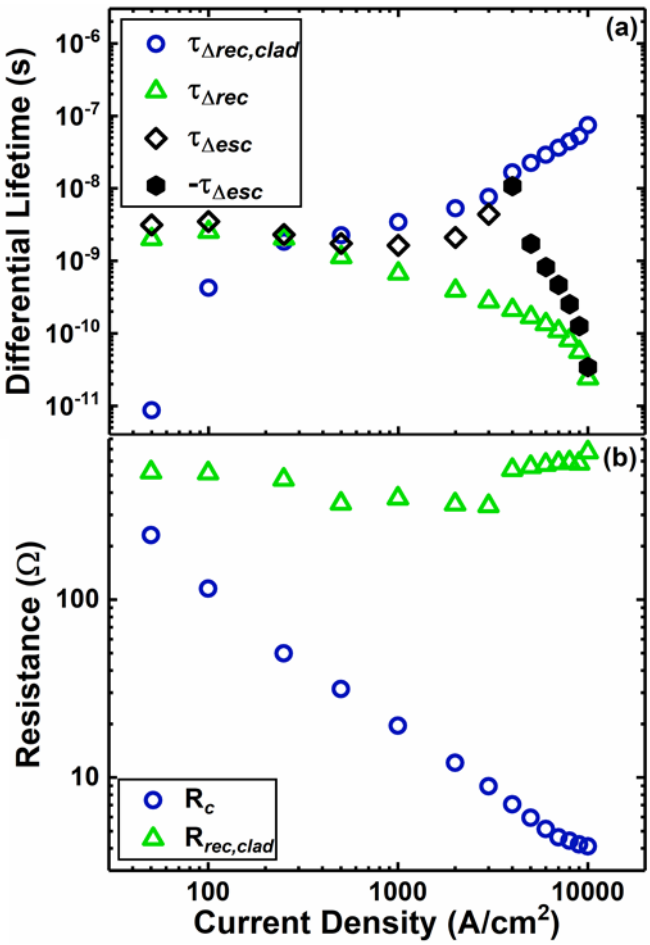

Figure 5.2 (a) DLT, absolute value of the net differential escape time, and differential recombination lifetime in the cladding layers as a function of current density. Open diamonds when $\tau_{\Delta esc}$ is dominated by leakage (positive $\tau_{\Delta esc}$) and closed hexagons when $\tau_{\Delta esc}$ is dominated by Coulomb-enhanced capture (negative $\tau_{\Delta esc}$). (b) Resistances associated with differential unconfined carriers in the cladding layers (R_c) and differential unconfined carriers that recombine in the cladding layers ($R_{rec,clad}$).

Figure 5.25.2 (b) shows the resistances associated with the number of differential unconfined carriers in the cladding (R_c) and the number of differential carriers that recombine in the cladding ($R_{rec,clad}$) as a function of current density. R_c is inversely proportional to the injected current (number of carriers), indicating that the number of unconfined carriers in the cladding increases with higher current density, as expected. However, $R_{rec,clad}$ has a weak dependency on current density, indicating that the recombination in the claddings is almost independent of carrier injection.

The differential and total injection efficiencies as a function of current density were calculated using the extracted parameters shown in Figure 5.25.2 (a) and Eqs. (5.6) and (5.7),

respectively, and are shown in Figure 5.3 (a). The differential injection efficiency at zero bias required to calculate the integral in Eq. (5.7) was estimated to be 0.33 by extrapolating the data in Figure 5.3. The total injection efficiency is generally lower than the differential injection efficiency. The injection efficiency is 0.45 at a current density of 50 A/cm^2 and becomes 0.97 at a current density of 10 kA/cm^2. According to Figure 5.25.2 (a), the term $\frac{\tau_{\Delta rec}}{\tau_{\Delta esc}}$ decreases with increasing current density because the net differential carrier escape lifetime from the QW increases and eventually becomes negative due to Coulomb-enhanced capture. At the same time, the differential recombination lifetime in the QW decreases, consuming the carriers before they leak out into the cladding layer. The combination of Coulomb-enhanced capture and faster carrier recombination in the QW ensures that the QW efficiently consumes carriers, leading to lower carrier leakage at high current densities. Similarly, due to the constant rate of recombination in the cladding with current density, at high current densities a smaller fraction of the terminal current recombines in the cladding ($\frac{R_c}{R_{clad-rec}} \approx 0$), as indicated in Figure 5.25.2 (b), and the effect of cladding recombination on the injection efficiency is reduced. The increase of injection efficiency with current density found here supports that injection-related mechanisms are not the cause of efficiency droop in the present LEDs. This finding is consistent with previous findings that show carrier leakage only affects the efficiency at low current densities.[14] Other studies also concluded that carrier leakage does not explain efficiency droop based on the failure of a temperature-dependent leakage model to reproduce droop [83,84]. Moreover, some studies experimentally observed higher droop at lower temperatures (which is inconsistent with a leakage model) and proposed saturation of the radiative rate[7] and asymmetric carrier transport [85] as potential causes of efficiency droop. Furthermore, although not presented here, we have observed similar injection efficiency trends for *c*-plane (0001) and *m*-plane ($10\bar{1}0$) LEDs, suggesting that the behavior of higher injection efficiency with higher current densities is not strongly orientation dependent.

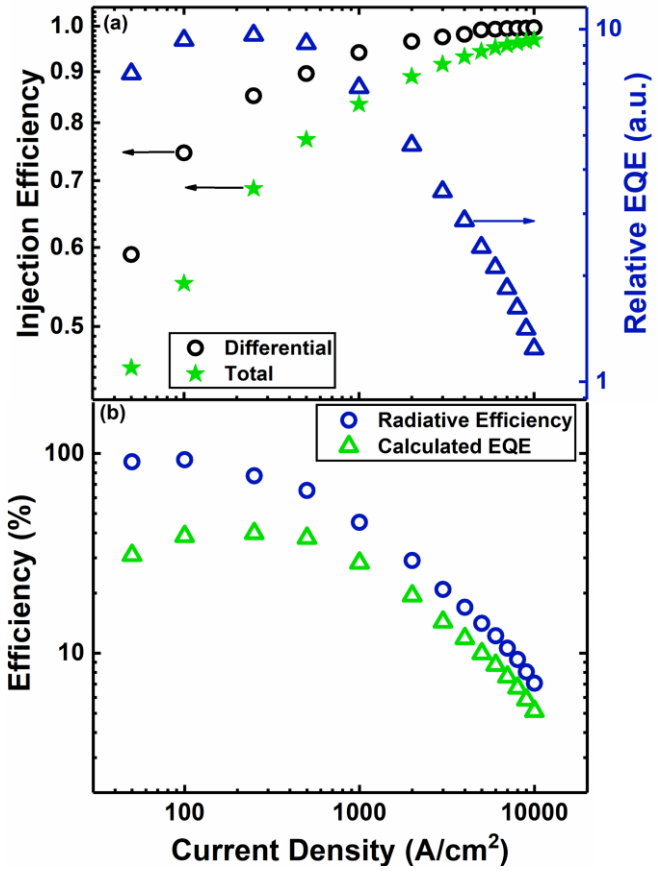

Figure 5.3 (a) Differential and total injection efficiencies and measured relative EQE as a function of current density. (b) Radiative efficiency and calculated absolute EQE as a function of current density.

The relative external quantum efficiency (EQE) was measured into a photodetector under CW conditions and is shown in Figure 5.3 (a). The peak EQE occurs at a current density of 250 A/cm^2. Using the injection efficiency and relative EQE, the relative radiative efficiency (η_r) is determined from $\eta_{EQE} = \eta_{LEE}\eta_{inj}\eta_r$, where $\eta_{IQE} = \eta_{inj}\eta_r$ and a constant light extraction efficiency (η_{LEE}) is assumed. This yields the shape of the radiative efficiency curve after accounting for injection efficiency. To obtain the absolute value of the radiative efficiency, the peak radiative efficiency is assigned a value of 93% based on previous low temperature/room temperature photoluminescence (PL) measurements on this LED [76]. Figure 5.3 (b) shows that the peak radiative efficiency occurs near a current density of 50 A/cm^2, which is lower than the peak of the relative EQE (250 A/cm^2) due to injection effects. The reduction of the radiative efficiency with increasing current density is consistent with an Auger model for efficiency droop [64,65]. The values of injection efficiency obtained here are also consistent with the absolute EQE values

measured for other 12-nm-thick SQW semipolar ($20\bar{2}\bar{1}$) LEDs grown using the same MOCVD system. For example, Pan *et al* [86]. reported a peak EQE of 52% and η_{LEE} = 75% for a 12-nm-thick SQW semipolar ($20\bar{2}\bar{1}$) LED. Here, we estimate the absolute EQE from $\eta_{EQE} = \eta_{LEE}\eta_{inj}\eta_r$ using the radiative efficiency in Figure (b) and assuming η_{LEE} = 75% if similar packaging is used. The calculated absolute EQE is shown in Figure 5.3 (b). The peak EQE is 40% (i.e., η_{EQE} = (0.75)(0.69)(0.78) = 0.40), which is similar to that reported by Pan *et al* [86].

To further clarify the effects of Coulomb-enhanced capture, recombination in the QW, and recombination in the cladding layers on injection efficiency, we calculate the total number of carriers in the QW (N_w) and total number of carriers in the claddings (N_c). Solving Eqs. (5.3) and (5.4) for N_w and N_c leads to:

$$N_w = \frac{1}{q}\int \eta_{\Delta inj}\tau_{\Delta rec}dI \tag{5.8}$$

$$N_c = \frac{1}{q}\int (1-\eta_{\Delta inj})\tau_{\Delta rec,clad}dI \tag{5.9}.$$

Figure 5.4 (a) shows N_w and N_c as a function of current density calculated using the parameters in Figure 5.25.2 (a) and Figure 5.3 (a). At low current densities, the carrier population in the QW is higher than that in the cladding layers due to the lower rate of recombination in the QW according to Figure 5.25.2 (a). The higher population of carriers in the QW at low current densities is responsible for the higher leakage observed at low current densities in Figure 5.25.2 (a). As the current density increases, N_w and N_c approach the same value. Conversely, N_c increases with increasing current density due to the higher recombination lifetime in the claddings at higher injection ($\tau_{\Delta rec,clad}$ in Figure 5.25.2 (a)). According to Figure 5.25.2 (a) and Figure 5.4 (a), the onset of Coulomb-enhanced capture occurs at the current density where N_c is of the same order of magnitude as N_w. Similar carrier populations in the QW and cladding layers makes carrier escape from the QW harder due to Coulomb repulsion. David *et al*.[45] also showed that the Coulomb-enhanced capture rate has a linear dependence on the carrier density in the claddings. According to Figure 5.25.2 (a) and Figure 5.4 (a), we observe a similar dependency for Coulomb-enhanced capture in our study.

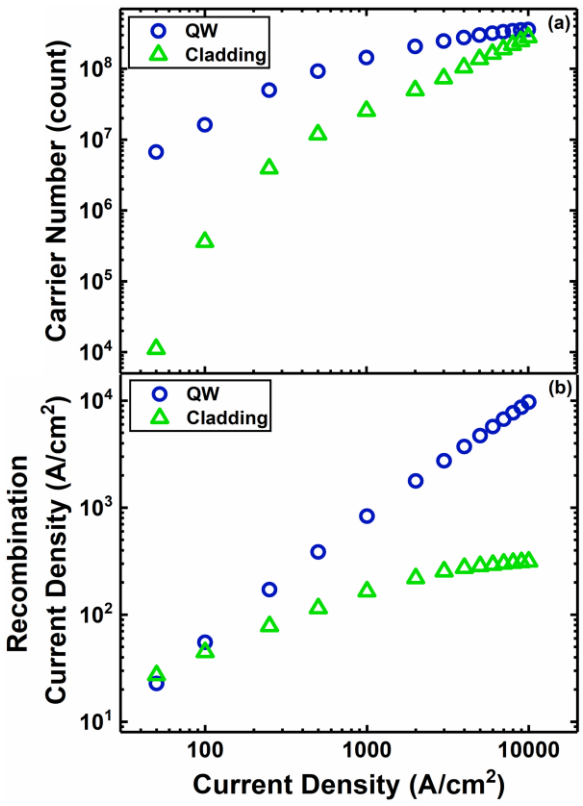

Figure 5.4 (a) Total number of carriers in the QW (N_w) and in the claddings (N_c) as a function of current density. (b) Recombination current density in the QW (J_w) and in the claddings (J_c).

We further investigate the effect of lifetimes and carrier population in different regions on the injection efficiency by calculating the recombination current densities in the QW and cladding layers. Using Eqs. (5.3), (5.4), and (5.6) the total recombination current density in the QW and cladding layers are:

$$J_w = \int dJ_w = \int q \frac{dN_w}{A\tau_{\Delta rec}} = \int \eta_{\Delta inj} dJ \tag{5.10}$$

$$J_c = \int dJ_c = \int q \frac{dN_c}{A\tau_{\Delta rec,clad}} = \int (1 - \eta_{\Delta inj}) dJ \tag{5.11}$$

where A is the area of the circular mesa and J_w and J_c are the total recombination current densities in the QW and cladding layers, respectively. Figure 5.4 (b) shows the recombination current densities in the QW and cladding layers. J_w has a stronger dependence on the injected current density than J_c, causing the recombination current density in the QW to be almost two

orders of magnitude higher than the recombination current density in the cladding at high current densities, resulting in an injection efficiency of nearly one. However, at low current densities the recombination current is divided between the QW and cladding layers leading to a lower injection efficiency. The weaker dependency of recombination current in the cladding layers on the injected current density results from the increasing $\tau_{rec,clad}$ being compensated by an increasing number of carriers in the cladding, as shown in Figure 5.25.2 (a) and Figure 5.4 (a), respectively.

In summary, we determined the injection efficiency of SQW semipolar $(20\bar{2}\bar{1})$ InGaN/GaN LEDs using our carrier rate equation approach and RF measurement technique. The small-signal equivalent circuit of the LED was derived using the differential rate equations. The DLT, net differential carrier escape time, and differential recombination lifetime in the cladding layers were extracted and used to determine the differential and total injection efficiencies. The injection efficiency is low at low current densities due to carrier leakage, but becomes approximately one at high injections due to the domination of carrier leakage by a Coulomb-enhanced capture process and higher recombination rate in the QW. The high recombination rate in the QW causes the carrier number in the QW to increase by a slower rate with increasing current density compared to the carrier number in the cladding layers. However, the recombination current density in the QW grows faster than that in the cladding, leading to the injection efficiency increasing with current density. The rise in the injection efficiency with increasing current density and the high injection efficiency at high current densities rules out injection-related mechanisms (e.g., carrier leakage and/or ballistic overshoot) as the primary cause of efficiency droop in the present InGaN/GaN LEDs.

5.2. Origin of efficiency and thermal droop in InGaN/GaN LEDs

Studies of droop are mostly based on a mathematical method known as ABC model. This model describes the behavior of internal quantum efficiency (IQE) of the LED and its most advanced form is $IQE = \frac{Bn^2}{An+Bn^2+Cn^3+f(n)}$ where n is carrier density in the QW, A is Shockley-Read-Hall (SRH) recombination coefficient, B is bimolecular recombination coefficient, C is Auger non-radiative recombination coefficient, and $f(n)$ represents the carrier leakage from QWs [87]. It is

observed that B and C reduce with increasing n which it is explained by phase space filling theory [88]. This method has several fundamental issues. First, there are too many unknown parameters in the equation for fitting IQE vs. n curve. Second, under optical pumping, estimation of n is difficult unless detailed absorption properties of epitaxial layers are known. Third, the diode does not reach flat band conditions under optical pumping and carriers do not experience the transport delay in the cladding that they experience under electrical injection [42]. On the other hand, some papers reported estimation of n under electrical injection by measuring the electrical -3dB bandwidth of LED and calculating the associated differential carrier lifetime (DLT) ($\tau = \frac{1}{2\pi f_{-3dB}}$). Then, DLT is used to calculated the carrier density in the QW [77,80]. However, there are inaccuracies in n since the total lifetime obtained from -3dB bandwidth is assumed to be solely from the recombination in the QW and transport delays and carrier leakage are neglected. Moreover, injection efficiency is assumed to be one meaning all the injected carriers recombine in the QW. Finally, -3dB bandwidth is measured under CW condition where internal heat can affect the carrier dynamics of the LED and consequently accurate determination of n.

Here, we use our rate equation approach and RF measurement technique to investigate the causes of efficiency and thermal droop. We use our newly developed pulsed-RF technique to measure the RF characteristics and study the carrier dynamics under isothermal condition. We used a temperature-controlled stage to study the cause of droop at elevated temperatures.

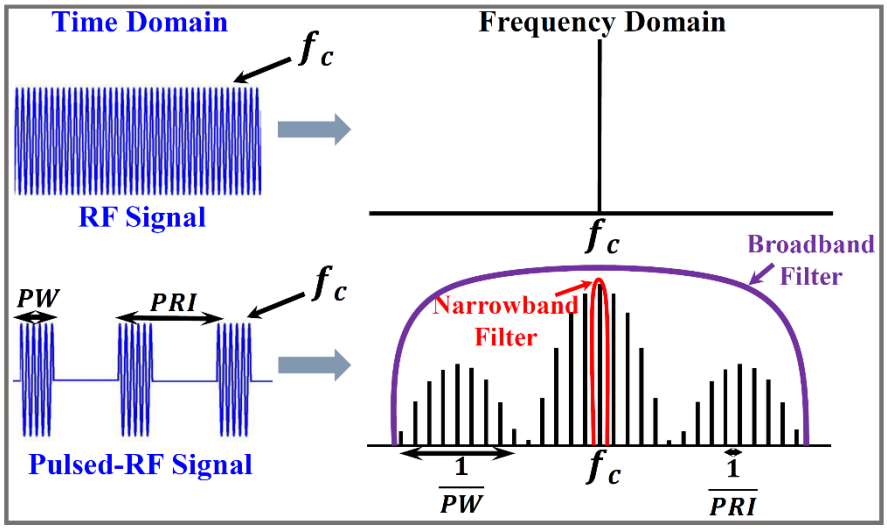

Figure 5.5 Concept of the pulsed-RF measurement developed to minimize the effect of self-heating on the measurements. A narrowband filter of the NA is used to pick the main harmonic of the RF frequency among all the generated harmonics.

To measure the modulation response and input impedance under isothermal condition, the LED is biased by DC pulses from a pulse generator with pulse repetition interval (PRI) of 10 µsec and pulse width (PW) of 1 µsec. Then, a small AC signal from a network analyzer (NA) is added to the DC pulses and sent to the LED. The reflected AC signal from the LED is used by NA to determine the input impedance of the device. To generate the modulation response, the output light of the LED is collected by an optical fiber and converted to electrical signal by a photodetector. The photodetector signal is amplified by a low noise amplifier and sent back to the NA. The received signals by NA are in the form of a pulsed-RF signal due to the LED being off during the off-state of the pulse. Figure 5.5 shows the transmitted (RF signal) and received (pulsed-RF signal) signals by the NA both in time and frequency domains. Unlike continuous-wave (CW) mode that NA receives signals with the same frequency (f_c) as the signal that it sends to the LED, in pulse mode the energy of the signal is spread out into infinite harmonics of the main frequency (f_c). To receive the main signal back, a very broadband receiver (few hundreds of MHz in this case) is required to collect all the harmonics where they interfere constructively and generate the main signal. This is almost impossible since such a broadband receiver still does not exist in the state-of-the-art NAs. However, we use a narrowband filter to pick only the central harmonic of the signal among all the generated harmonics (see Figure 5.5) since it has the same frequency as the input signal. Although most of the energy of the signal would be lost to the rest of the harmonics, the main frequency can be detected similar to the CW

mode enabling data evaluation by the NA. The only drawback of this technique compared with CW mode is the power loss which it can be ratio out. Mathematically, it can be shown that the fraction of energy of the main harmonic compared with the total energy of the signal is equal to the pulse duty cycle. Selection of the narrowband filter depends on the pulse frequency since the spacing between the two adjacent harmonics is equal to the pulse frequency (see Figure 5.5).

Modulation response and input impedance of the LED are measured using the pulsed-RF technique at current densities of 10 A/cm^2 to 10 kA/cm^2 and at different stage temperatures. Figure 5.6 (a) shows the electrical -3dB bandwidth of the LED as a function of current density for different stage temperatures. Electrical -3dB bandwidth increases with increase of current density mainly due to the increase of spontaneous emission [42]. Similar to RF measurements, relative external quantum efficiency (EQE) of the LED was measured under the same pulse conditions at the same current densities and stage temperatures (see Figure 5.6 (b)). Although the EQE is strongly affected by temperature which is widely known as thermal droop, the RF characteristics have a weak dependency on temperature.

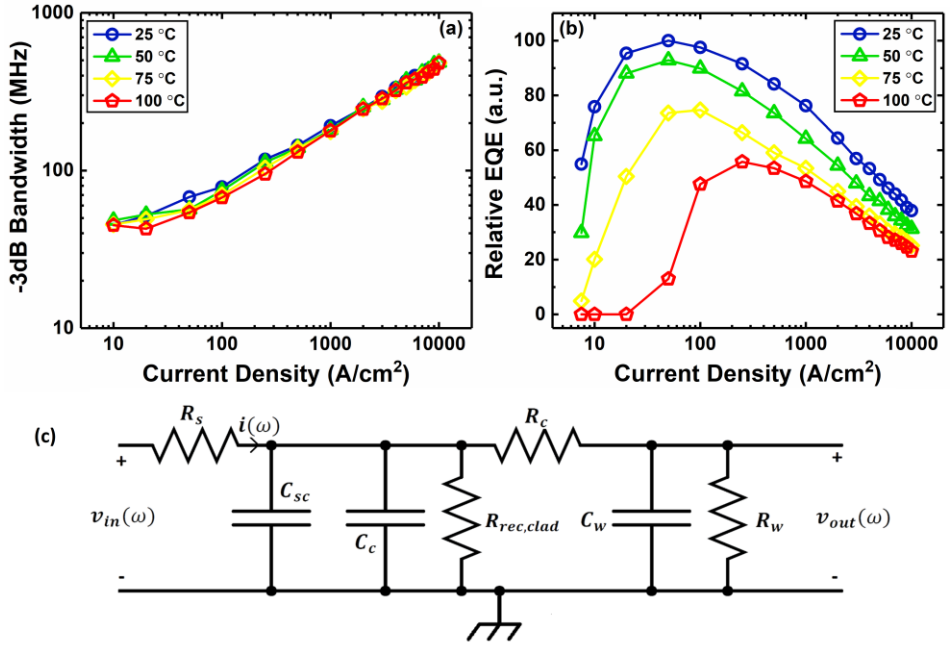

Figure 5.6 (a) Electrical -3dB bandwidth and, (b) relative EQE of the LED as a function of current density at different stage temperatures. (c) the equivalent electrical circuit of the LED.

The DLT, net differential carrier escape time, and differential recombination lifetime and transport time in the cladding regions were extracted as a function of current density and stage temperature after simultaneous fit of modulation response and input impedance of the circuit of Figure 5.6 (c) to the measured modulation response and input impedance of the LED for the frequency range of 10 MHz to 2 GHz. Examples of the goodness of fittings and verification of the model are shown in our previous works [42,89]. Figure 5.7 (a) shows the DLT ($\tau_{\Delta rec}$) as a function of current density at different stage temperatures. DLT reduces with increasing current density but it is almost independent of temperature. David *et al.* [45] have reported similar dependencies for DLT obtained by an electrical technique. Injection efficiency and carrier density in the QW are calculated using extracted lifetimes and are depicted in Figure 5.7 (b) and Figure 5.7 (c), respectively. The injection efficiency at all temperatures increases with current density and eventually approaches one. We conclude that the injection efficiency is not the cause of efficiency and thermal droop. The carrier density in the QW increases with increase of current density. Detailed discussion on the behavior of injection efficiency and carrier density can be found in our previous work [90]. The radiative efficiency (η_r) in Figure 5.7 (d) is extracted using relative EQE (η_{EQE}) of Figure 5.6 (b) and injection efficiency (η_{inj}) in Figure 5.7 (b) by assuming a constant extraction efficiency (η_{ext}) in $\eta_{EQE} = \eta_{ext}\eta_{inj}\eta_r$. To adjust the η_r curves to absolute values, we set the peak of η_r data at temperature of 25 °C to 93% which was measured for this sample using room-temperature/low-temperature PL technique [76]. The rest of the curves were adjusted relative to the η_r at 25 °C. However, the main conclusions of this study are independent of the absolute peak of η_r and the trends remain similar at lower values of η_r peak.

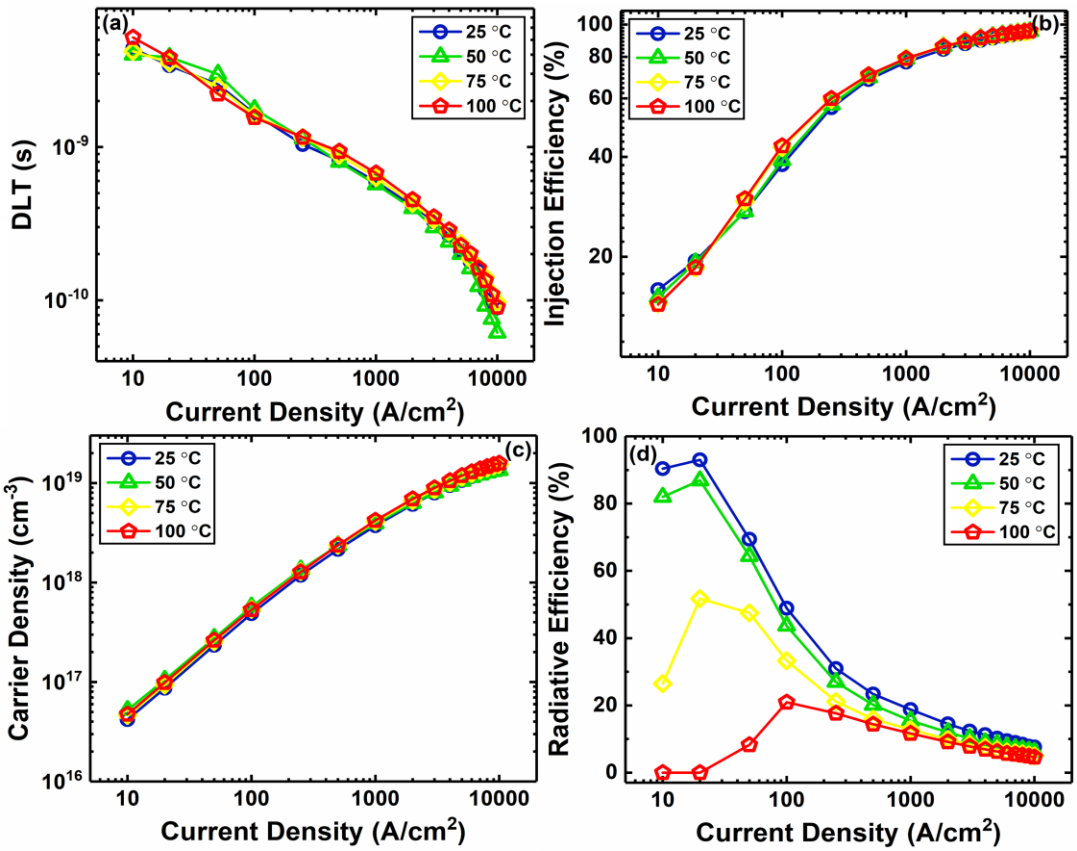

Figure 5.7 (a) DLT, (b) injection efficiency, (c) carrier density in the QW, and (d) radiative efficiency as a function of current density at different stage temperatures.

Knowing the η_r, η_{inj}, and DLT from Figure , differential radiative ($\tau_{\Delta r}$) and non-radiative ($\tau_{\Delta nr}$) lifetimes in the QW are extracted using the following equations [80]:

$$\tau_{\Delta r}^{-1} = \eta_r \tau_{\Delta rec}^{-1} + G\frac{d\eta_r}{dn} \tag{5.12}$$

$$\tau_{\Delta nr}^{-1} = (1-\eta_r)\tau_{\Delta rec}^{-1} - G\frac{d\eta_r}{dn} \tag{5.13}$$

$$G = \frac{\eta_{inj} J}{qd} \tag{5.14}$$

where $\tau_{\Delta rec}$, G, J, d, and q are DLT, generation rate in the QW, injected current density, QW thickness, and electron charge, respectively.

Figure 8 (a) and (b) are differential radiative and non-radiative lifetimes at various current densities for different stage temperatures. Non-radiative lifetime compared to radiative lifetime reduces drastically with increasing current density. This means at high current densities the extra injected carriers into the QW are more likely to end up in the non-radiative process. A recent theoretical calculation of radiative and Auger lifetimes vs. carrier density shows similar dependencies where the Auger lifetime has a stronger dependency on carrier density compared to radiative lifetime [91]. At higher temperatures, the radiative lifetime increases at all current densities while the non-radiative lifetime decreases only at low current densities and it is almost independent of temperature at high current densities. We attribute the non-radiative lifetime at low current densities to SRH recombination. The SRH lifetime (τ_{SRH}) is related to temperature through [92]:

$$\tau_{SRH} = \tau_0(1 + cosh\frac{E_T - E_{Fi}}{kT}) \tag{5.15}$$

where τ_0 is a constant related to trap densities, E_T is the energy of the traps, and E_{Fi} is the intrinsic fermi level. Due to linear dependence of SRH recombination rate on carrier density, total and differential SRH lifetimes are equal. Therefore, we extracted the SRH lifetime as the non-radiative lifetime at the lowest current density (10 A/cm^2) by assuming the Auger recombination is negligible [80]. Inset of Figure (b) shows the SRH lifetime and the theoretical fitting of Eq. (5.15) as a function of temperature. This is similar to the SRH lifetime reported by Nguyen *et al.* [93] and Meyaard *et al.* [87] obtained from optical measurements.

Figure (c) and (d) are the total radiative (R_r) and non-radiative (R_{nr}) recombination rates in the QW calculated using Eqs. (5.16) and (5.17), carrier density in the QW (Figure 5.7 (c)), and differential radiative and non-radiative lifetimes (Figure 5.8 (a) and (b)).

$$R_r = \int \frac{dn}{\tau_{\Delta r}} \tag{5.16}$$

$$R_{nr} = \int \frac{dn}{\tau_{\Delta nr}} \tag{5.17}$$

Both rates increase with increasing current density with non-radiative rate by a higher slope and radiative rate tending to saturate. Therefore, a combination of higher non-radiative

recombination rate and saturation of radiative rate leads to efficiency droop. Moreover, radiative rate reduces with temperature at all current densities while the non-radiative rate increases with temperature only at low current densities. The temperature dependency of radiative process is aligned with theoretical work of Kioupakis *et al.* [94] and experimental reports [95]. The stronger temperature dependency of non-radiative rate at low current density is attributed to the SRH recombination while the weaker dependency on temperature at high current densities is due to indirect Auger process. Kioupakis *et al.* [96] theoretically showed that the Auger process in nitride LEDs is a result of indirect scattering processes with weaker dependency on temperature compared to direct Auger. Thus, thermal droop is caused by decrease of radiative rate and increase of SRH recombination with increasing temperature.

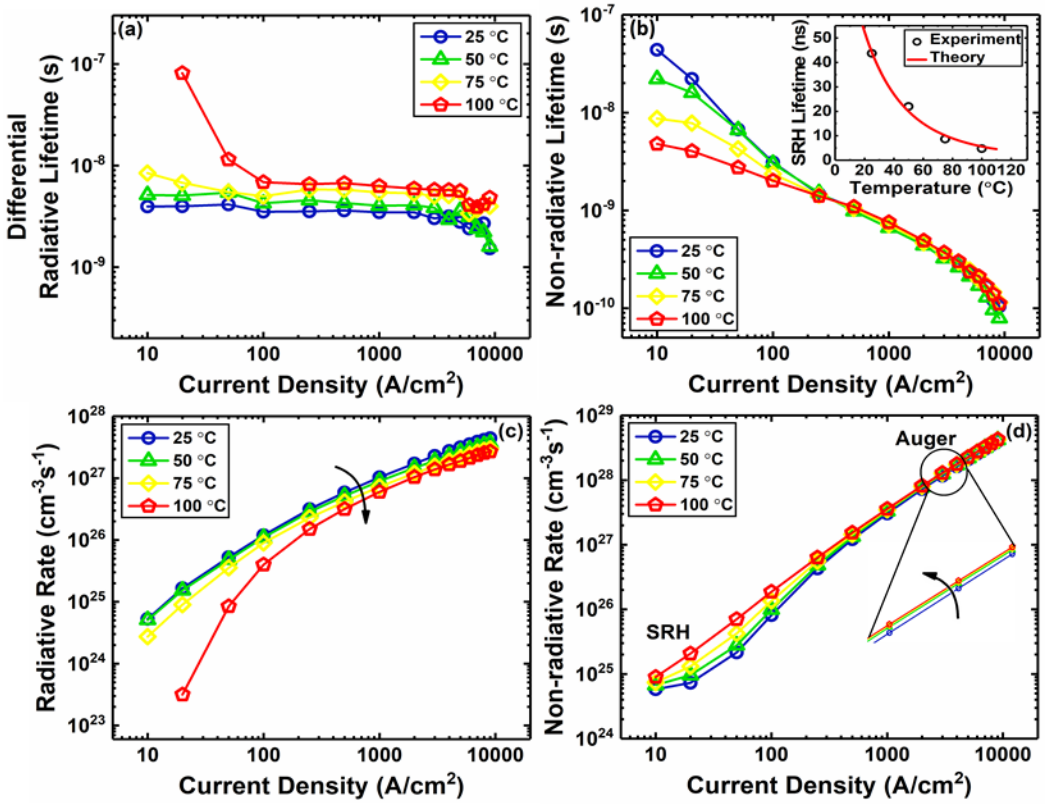

Figure 5.8 (a) Differential radiative and (b) non-radiative lifetimes, and (c) total radiative and (d) non-radiative recombination rates vs. current density for different stage temperatures. Inset of (b) is SRH lifetime at various temperatures.

In conclusion, we have studied origin of efficiency and thermal droop in electrically injected SQW InGaN/GaN LEDs using a rate equation approach and a pulsed-RF measurement

technique. The pulsed-RF measurement technique enabled the characterization of the LEDs under isothermal conditions to avoid the effects of self-heating on the study of carrier dynamics. Rate equations considering dominant carrier processes under electrical injection were used to derive the equivalent electrical circuit of the LEDs. The circuit was used to fit the RF characteristics of the LED which yielded the DLT, net differential carrier escape time, and differential recombination lifetime and transport time in the cladding regions. Injection efficiency, carrier density in the QW, differential radiative and non-radiative lifetimes and total radiative and non-radiative rates were extracted as a function of current density and stage temperature. The injection efficiency is less than one at low current densities and it approaches one at high current densities. We conclude that the injection efficiency is not the primary cause of efficiency or thermal droop. Efficiency droop is caused by Auger recombination process where its weak dependency on temperature suggests that it is indirect. Thermal droop is due to increase of SRH and reduction of radiative recombination at higher temperatures.

6. Summary of Achievements

During the three year project, we have developed a framework to study and optimize the modulation bandwidth and the efficiency of InGaN/GaN LEDs on selected nonpolar, semipolar and polar orientations. The overall achievements of the project are summarized below.

1. We presented a world record modulation bandwidth of 1.3 to 1.5 GHz at low current densities (200-500 A/cm^2). Previously, the highest reported modulation bandwidths related to c-plane LEDs were up to a GHz at 5-10 kA/cm^2.
2. For the first time, we performed a comparison of bandwidth *vs.* current density for nonpolar, semipolar and polar orientations. The study revealed that due to lack of QCSE in nonpolar, we can obtain GHz bandwidth at very low current densities (~ 100 A/cm^2) where efficiency droop, thermal droop, and power consumption is minimized which results in a higher BEFOM for nonpolar LEDs.
3. A rate-equation-based modeling to account for carrier dynamics in InGaN/GaN LEDs under electrical injection was developed throughout the project. We were able to obtain various recombination and escape rates by simultaneous fitting of RF data (impedance and S_{21}).

4. We developed the first pulsed-RF measurement setup to study carrier dynamics under isothermal condition.
5. We evaluated the recombination coefficients of semipolar InGaN/GaN LEDs using a differential lifetime analysis based on our RF measurement tool. The study revealed that low auger coefficient (C) is responsible for the observed lower droop in the semipolar LED compared to c-plane LED.
6. A systematic evaluation of recombination rates using our developed rate-equation based modeling under isothermal condition revealed the cause of efficiency and thermal droop in InGaN/GaN LEDs which had been subject of debate in the past decades. We were also able to determine the injection efficiency and corresponding radiative efficiency of InGaN/GaN LEDs using our rate-equation based modeling. Our findings excluded the injection efficiency as the primary cause of efficiency droop.
7. We explored the trade-off between modulation bandwidth and efficiency of InGaN/GaN LEDs for the first time. We suggested a figure of merit that accounts for both bandwidth and efficiency (BEFOM as described in section 4) for dual illumination and communication applications. Our study develops a platform to understand various mechanisms responsible for bandwidth/efficiency limitations at different current density ranges which allows for co-optimization of bandwidth and efficiency in InGaN/LEDs for VLC.
8. One student (Dr. Arman Rashidi) received his Ph.D. working entirely on this funded DOD project.
9. We published eight journal articles, with one more under review, and a comprehensive review of the field under preparation for *Laser and Photonics Reviews*. We also gave more than 11 conference presentations, with six of these as invited talks.

7. Future Work

With the work we have accomplished thus far we have discovered several new ideas and methods for improving III-N LEDs for VLC. Two of the many important aspects in achieving high modulation bandwidth and efficiency is the design and optimization of the active region and device geometry. Typical active region designs for blue (450nm) emission consist of InGaN

single and multiple quantum well configurations. By designing the composition, QW thickness, barrier thickness and QW number the modulation bandwidth and efficiency may be tailored for specific applications. An additional consideration for improvement is the device design geometry itself. By moving towards alternative device geometries, the bandwidth and efficiency may be increased due to the advantages of such designs. Such designs include flip-chip LEDs (FCLED) and array configurations. As shown, there is substantial room for improving III-N LEDS for VLC applications. *The new techniques developed here can also be applied to understanding the present efficiency limitations of UV and green LEDs.* In the following section our future work will be described in detail on how we may pursue higher performance and reliability.

7.1 Active Region Design

The active region is an important aspect of the design for high speed LEDs. Typical active region designs consist of InGaN single or multiple quantum wells [97–99]. Based on the composition percentage, well thickness, barrier thickness, and quantum well number the spontaneous wavelength emission can be designed. As shown previously, carrier injection is a crucial aspect for achieving high modulation bandwidths. Carriers are injected into the quantum wells at depending on drift and diffusion from the barriers. As a carrier is modulated the rate of injection along with the recombination rate determines how fast the signal can be modulated. The active region can be modeled by defining rate equations for each quantum well in a active region. In figure 7.1 (b), the band structure and rate equations for a three quantum wells is shown. By solving the coupled rate equations, the modulation bandwidth may be modeled as shown in Figure 7.1(a). Therefore, different active region designs may be studied to determine the most desirable performance. In high speed LED there has been shown to be a tradeoff between high speed modulation bandwidth and quantum efficiency [100]. As carriers are injected into the active region, some recombine to form spontaneous emission photons, and others recombine non-radiative or are thermally excited out of the quantum well. Thus, it would be worthwhile to investigate the tradeoff between bandwidth and efficiency with a comparison between designs with differing quantum wells. Figure 7.2 shows three active region designs we'd like to investigate. It is expected that the single quantum will have a faster bandwidth comparted to multiple QW devices. However, the multiple QW structures should yield higher efficiency. By

comparing these designs we can validate the model formulated by the rate equations, and we will gain some good insight into the bandwidth efficiency trade off. By demonstrating a valid model we can develop some metrics for the proper design of high speed/ high efficiency LEDs for VLC.

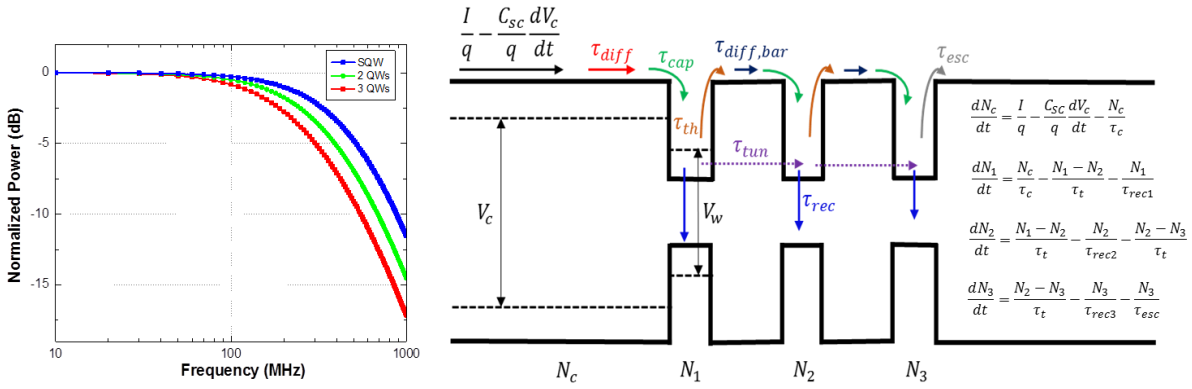

Figure 7.1 (a) Bandwidth Simulation of 1,2, and 3 QW structures (b) Band diagram of three quantum well structure with individual quantum well rate equations.

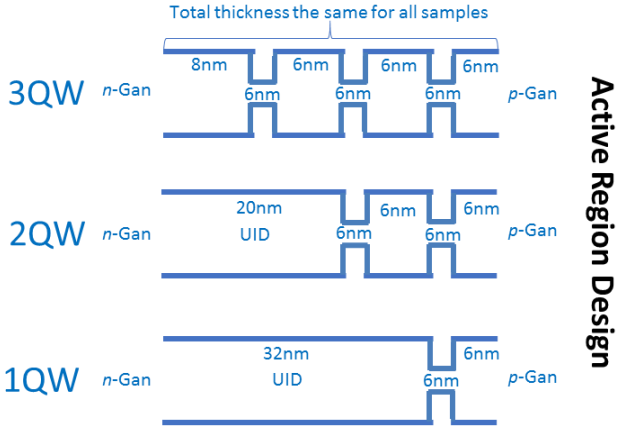

Figure 7.2 High Speed LED Quantum Well Structure Design

7.2. Device Design Flip Chip

A move towards alternate designs is being considered in order to achieve higher modulation bandwidth and optical output power. One such design utilizes a flip-chip structure. Some advantages of this structure include better heat management, increase light extraction, and better current spreading in the *p*-GaN contact. A Schematic of our flip-chip design is shown in Figure 7.3. The use of high thermally conductive sub-mounts allows heat generated in the active region of the devices to be dissipated quicker. Therefore, the effects of thermal droop on the efficiency and bandwidth of the devices will be reduced when operating the devices in a CW mode. Also, the flip chip may be designed by optimizing a half cavity for an increased light extraction. By placing the maximum of the standing wave electric field on the active region the output power has been shown to increase by more than two times [99]. Additionally, by bonding the *p*-GaN directly to metal there will be no need for a conductive/transparent ITO layer. This will increase the current spreading and ensure a more uniform distribution of current. A simulation using COMSOL, Figure 7.4, verifies the current spreading through the *p*-contact and through the active region for our flip-chip design. The advantages described by moving to this device structure may show promising results for achieving very high performance III-N LEDs for VLC applications.

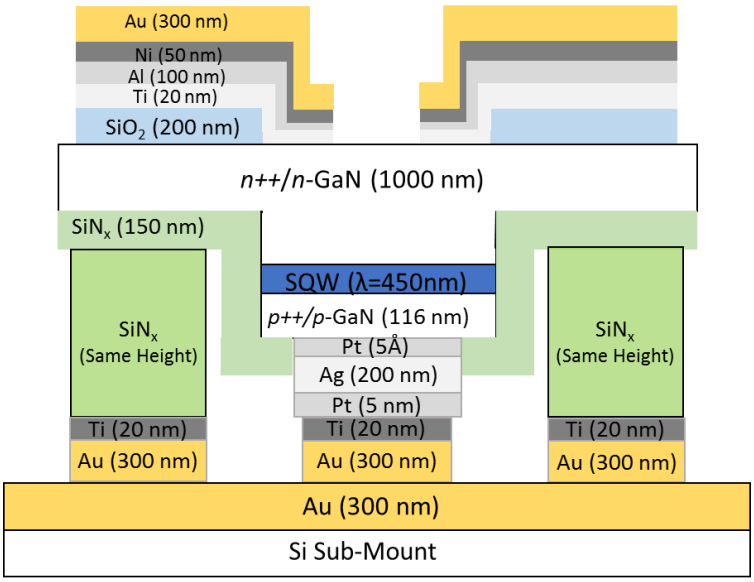

Figure 7.3 High Speed Flip Chip Design

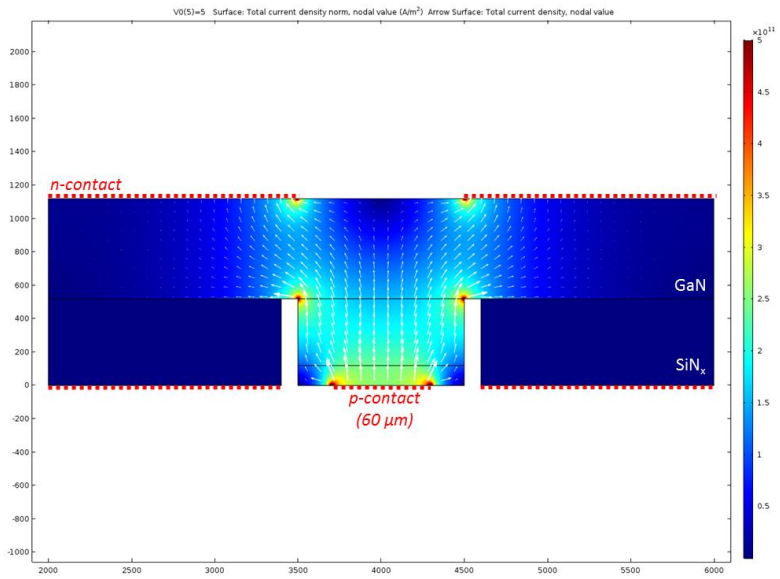

Figure 7.4 COMSOL High Speed LED Current Distribution Simulation

7.3. Arrays

The implementation of micro LED arrays is of particular interest because of the limited output power of micro-LEDs vs larger standard LEDs. To achieve high modulation bandwidth, the RC limited bandwidth of the LED must be less than the carrier lifetime limited bandwidth. Thus, the device geometry must maintain a small size to ensure this requirement. However, small devices are limited to the amount of total output power at equivalent voltages compared to larger devices. One design to achieve high modulation bandwidth and high output power is an array design. By designing arrays of several individual μ-LEDs, the total output power can be increased as well as maintain a high modulation bandwidth. The array may be configured in series or parallel designs. Series designs will ensure uniform current through all devices but will require a large supply voltage to turn on all the devices. The parallel configuration does not require such large voltages, but uniform current distribution may be difficult to achieve across all devices due to small differences in device fabrication. Another aspect that must be considered is the total RC bandwidth of all the interconnects and testing pads on array devices. The RC bandwidth will be limited not only by each individual μ-LED, but also the total array interconnects and probing pads. Methods such a transmission line impedance matching can be designed in order to ensure a low RC limited bandwidth.

7.4. BW/QW co-optimization

The two important performance figures of merit for high speed LEDs are frequency bandwidth and efficiency. However, there is a tradeoff between high speed and high efficiency [100]. The development of multiple quantum well high speed LEDs can provide high efficiency/ high output power, but the bandwidth of multiple quantum well structures also suffers from carrier transport delays from well to well. Since the total bandwidth of multi-quantum well LEDs is dependent on transport and recombination times, the total bandwidth will reduce with the addition of subsequent QWs compared to a single QW device. Therefore, it is expected that the highest modulation bandwidths can be achieved by using single quantum well structures. Yet, the efficiency of a single quantum well is expected to be lower than that of multiple QW structures due to an increased amount of carriers escaping the single well. One such approach that may yield high speed and high output power is implementing half cavity designs such as the flip-chip LED (FCLED) discussed previously. The epitaxial layer may consist of a single quantum well with a p-GaN contact/reflector. By using a single quantum the total bandwidth will not be reduced as in multiple quantum wells due to transport time delays. However, the extraction efficiency may be increased by implementing a half cavity design with proper placement of the active region with the reflection pattern from the metallic contact/mirror. Thus, a properly designed FCLED may be able to incorporate both high speed and high output power. Therefore, by studying different cavity designs and device geometries we may be able to design a high speed and efficiency LED for VLC applications.

References

[1] G. Cossu, R. Corsini, A.M. Khalid, S. Balestrino, A. Coppelli, A. Caiti, and E. Ciaramella, in *2013 2nd Int. Workshop Opt. Wirel. Commun. IWOW* (2013), pp. 11–15.

[2] A. Baranov and E. Tournie, *Semiconductor Lasers: Fundamentals and Applications* (Elsevier, 2013).

[3] M.M. Dumitrescu, M.J. Saarinen, M.D. Guina, and M.V. Pessa, IEEE J. Sel. Top. Quantum Electron. **8**, 219 (2002).

[4] M. Akhter, P. Maaskant, B. Roycroft, B. Corbett, P. de Mierry, B. Beaumont, and K. Panzer, Electron. Lett. **38**, 1457 (2002).

[5] T. Matsuoka, T. Ito, and T. Kaino, Electron. Lett. **36**, 1836 (2000).

[6] J.W. Shi, K.L. Chi, J.M. Wun, J.E. Bowers, Y.H. Shih, and J.K. Sheu, IEEE Electron Device Lett. **37**, 894 (2016).
[7] R.X.G. Ferreira, E. Xie, J.J.D. McKendry, S. Rajbhandari, H. Chun, G. Faulkner, S. Watson, A.E. Kelly, E. Gu, R.V. Penty, I.H. White, D.C. O'Brien, and M.D. Dawson, IEEE Photonics Technol. Lett. **28**, 2023 (2016).
[8] F. Bernardini, V. Fiorentini, and D. Vanderbilt, Phys. Rev. B **56**, R10024 (1997).
[9] S. Rajbhandari, J.J.D. McKendry, J. Herrnsdorf, H. Chun, G. Faulkner, Harald Haas, I.M. Watson, D. O'Brien, and M.D. Dawson, Semicond. Sci. Technol. **32**, 023001 (2017).
[10] D. Rosales, B. Gil, T. Bretagnon, B. Guizal, F. Zhang, S. Okur, M. Monavarian, N. Izyumskaya, V. Avrutin, Ü. Özgür, H. Morkoç, and J.H. Leach, J. Appl. Phys. **115**, 073510 (2014).
[11] D. Rosales, B. Gil, T. Bretagnon, B. Guizal, N. Izyumskaya, M. Monavarian, F. Zhang, S. Okur, V. Avrutin, U. Ozgur, and H. Morkoç, J. Appl. Phys. **116**, 093517 (2014).
[12] C.A. Hurni, A. David, M.J. Cich, R.I. Aldaz, B. Ellis, K. Huang, A. Tyagi, R.A. DeLille, M.D. Craven, F.M. Steranka, and M.R. Krames, Appl. Phys. Lett. **106**, 031101 (2015).
[13] X.A. Cao, S.F. LeBoeuf, M.P. D'Evelyn, S.D. Arthur, J. Kretchmer, C.H. Yan, and Z.H. Yang, Appl. Phys. Lett. **84**, 4313 (2004).
[14] D.F. Feezell, J.S. Speck, S.P. DenBaars, and S. Nakamura, J. Disp. Technol. **9**, 190 (2013).
[15] J. Cho, E.F. Schubert, and J.K. Kim, Laser Photonics Rev. **7**, 408 (2013).
[16] C. Weisbuch, M. Piccardo, L. Martinelli, J. Iveland, J. Peretti, and J.S. Speck, Phys. Status Solidi A **212**, 899 (2015).
[17] J. Piprek, Phys. Status Solidi A **207**, 2217 (2010).
[18] A.E. Romanov, T.J. Baker, S. Nakamura, and J.S. Speck, J. Appl. Phys. **100**, 023522 (2006).
[19] S. Okur, M. Nami, A.K. Rishinaramangalam, S.H. Oh, S.P. DenBaars, S. Liu, I. Brener, and D.F. Feezell, Opt. Express **25**, 2178 (2017).
[20] A. Rashidi, M. Monavarian, A. Aragon, S. Okur, M. Nami, A. Rishinaramangalam, S. Mishkat-Ul-Masabih, and D. Feezell, IEEE Photonics Technol. Lett. **29**, 381 (2017).
[21] D.F. Feezell and M. Monavarian, (Unpublished).
[22] M. Monavarian, A. Rashidi, A. Aragon, S.H. Oh, M. Nami, S.P. DenBaars, and D. Feezell, Opt. Express **25**, 19343 (2017).
[23] A. Rashidi, M. Nami, M. Monavarian, A. Aragon, K. DaVico, F. Ayoub, S. Mishkat-Ul-Masabih, A. Rishinaramangalam, and D. Feezell, J. Appl. Phys. **122**, 035706 (2017).
[24] A. Rashidi, M. Monavarian, A. Aragon, and D. Feezell, (Unpublished).
[25] E. Kioupakis, Q. Yan, D. Steiauf, and C.G.V. de Walle, New J. Phys. **15**, 125006 (2013).
[26] E. Kioupakis, Q. Yan, and C.G.V. de Walle, Appl. Phys. Lett. **101**, 231107 (2012).
[27] S. Zhu, S. Lin, J. Li, Z. Yu, H. Cao, C. Yang, J. Li, and L. Zhao, Appl. Phys. Lett. **111**, 171105 (2017).
[28] A. David and M.J. Grundmann, Appl. Phys. Lett. **96**, 103504 (2010).
[29] D. Yevick and W. Streifer, Electron. Lett. **19**, 1012 (1983).
[30] C. Du, X. Huang, C. Jiang, X. Pu, Z. Zhao, L. Jing, W. Hu, and Z.L. Wang, Sci. Rep. **6**, 37132 (2016).
[31] B. Corbett, Z. Quan, D.V. Dinh, G. Kozlowski, D. O'Mahony, M. Akhter, S. Schulz, P. Parbrook, P. Maaskant, M. Caliebe, M. Hocker, K. Thonke, F. Scholz, M. Pristovsek, Y. Han, C.J. Humphreys, F. Brunner, M. Weyers, T.M. Meyer, and L. Lymperakis, in *Proceeding SPIE* (2016), p. 97681G.
[32] D.V. Dinh, Z. Quan, B. Roycroft, P.J. Parbrook, and B. Corbett, Opt. Lett. **41**, 5752 (2016).

[33] J.J.D. McKendry, R.P. Green, A.E. Kelly, Z. Gong, B. Guilhabert, D. Massoubre, E. Gu, and M.D. Dawson, IEEE Photonics Technol. Lett. **22**, 1346 (2010).
[34] C.L. Liao, Y.F. Chang, C.L. Ho, and M.C. Wu, IEEE Electron Device Lett. **34**, 611 (2013).
[35] Z. Quan, D.V. Dinh, S. Presa, B. Roycroft, A. Foley, M. Akhter, D. O'Mahony, P.P. Maaskant, M. Caliebe, F. Scholz, P.J. Parbrook, and B. Corbett, IEEE Photonics J. **8**, 1 (2016).
[36] C.H. Chen, M. Hargis, J.M. Woodall, M.R. Melloch, J.S. Reynolds, E. Yablonovitch, and W. Wang, Appl. Phys. Lett. **74**, 3140 (1999).
[37] D.V. Dinh, Z. Quan, B. Roycroft, P.J. Parbrook, and B. Corbett, Opt. Lett. **41**, 5752 (2016).
[38] J.-W. Shi, K.-L. Chi, J.-M. Wun, J.E. Bowers, Y.-H. Shih, and J.-K. Sheu, IEEE Electron Device Lett. **37**, 894 (2016).
[39] C.-L. Liao, C.-L. Ho, Y.-F. Chang, C.-H. Wu, and M.-C. Wu, IEEE Electron Device Lett. **35**, 563 (2014).
[40] J.-W. Shi, J.-K. Sheu, C.-H. Chen, G.-R. Lin, and W.-C. Lai, IEEE Electron Device Lett. **29**, 158 (2008).
[41] J.-M. Wun, C.-W. Lin, W. Chen, J.-K. Sheu, C.-L. Lin, Y.-L. Li, J.E. Bowers, J.-W. Shi, J. Vinogradov, and R. Kruglov, IEEE Photonics J. **4**, 1520 (2012).
[42] A. Rashidi, M. Nami, M. Monavarian, A. Aragon, K. DaVico, F. Ayoub, S. Mishkat-Ul-Masabih, A. Rishinaramangalam, and D. Feezell, J. Appl. Phys. **122**, 035706 (2017).
[43] L. Riuttanen, P. Kivisaari, N. Mäntyoja, J. Oksanen, M. Ali, S. Suihkonen, and M. Sopanen, Phys. Status Solidi C **10**, 327 (2013).
[44] M. Meneghini, N. Trivellin, G. Meneghesso, E. Zanoni, U. Zehnder, and B. Hahn, J. Appl. Phys. **106**, 114508 (2009).
[45] A. David, C.A. Hurni, N.G. Young, and M.D. Craven, Appl. Phys. Lett. **109**, 033504 (2016).
[46] C.H. Chen, M. Hargis, J.M. Woodall, M.R. Melloch, J.S. Reynolds, E. Yablonovitch, and W. Wang, Appl. Phys. Lett. **74**, 3140 (1999).
[47] M. Monavarian, A. Rashidi, A.A. Aragon, S.H. Oh, A.K. Rishinaramangalam, S.P. DenBaars, and D. Feezell, Appl. Phys. Lett. **112**, 041104 (2018).
[48] M. Monavarian, D. Rosales, B. Gil, N. Izyumskaya, S. Das, Ü. Özgür, H. Morkoç, and V. Avrutin, in *Proc SPIE* (2016), p. 974826.
[49] B. Corbett, Z. Quan, D.V. Dinh, G. Kozlowski, D. O'Mahony, M. Akhter, S. Schulz, P. Parbrook, P. Maaskant, M. Caliebe, M. Hocker, K. Thonke, F. Scholz, M. Pristovsek, Y. Han, C.J. Humphreys, F. Brunner, M. Weyers, T.M. Meyer, and L. Lymperakis, in *Proc SPIE* (2016), p. 97681G.
[50] A. Rashidi, M. Monavarian, A. Aragon, A. Rishinaramangalam, and D. Feezell, IEEE Electron Device Lett. **39**, 520 (2018).
[51] Y. Zhao, S. Tanaka, C.-C. Pan, K. Fujito, D. Feezell, J.S. Speck, S.P. DenBaars, and S. Nakamura, Appl. Phys. Express **4**, 082104 (2011).
[52] C.-C. Pan, S. Tanaka, F. Wu, Y. Zhao, J.S. Speck, S. Nakamura, S.P. DenBaars, and D. Feezell, Appl. Phys. Express **5**, 062103 (2012).
[53] D.F. Feezell, J.S. Speck, S.P. DenBaars, and S. Nakamura, J. Disp. Technol. **9**, 190 (2013).
[54] Y. Kawaguchi, C.-Y. Huang, Y.-R. Wu, Q. Yan, C.-C. Pan, Y. Zhao, S. Tanaka, K. Fujito, D. Feezell, C.G.V. de Walle, S.P. DenBaars, and S. Nakamaura, Appl. Phys. Lett. **100**, 231110 (2012).
[55] S. Marcinkevičius, R. Ivanov, Y. Zhao, S. Nakamaura, S.P. DenBaars, and J.S. Speck, Appl. Phys. Lett. **104**, 111113 (2014).

[56] S. Marcinkevičius, Y. Zhao, K.M. Kelchner, S. Nakamaura, S.P. DenBaars, and J.S. Speck, Appl. Phys. Lett. **103**, 131116 (2013).
[57] S.H. Oh, B.P. Yonkee, M. Cantore, R.M. Farrell, J.S. Speck, S. Nakamura, and S.P. DenBaars, Appl. Phys. Express **9**, 102102 (2016).
[58] A. David, C.A. Hurni, N.G. Young, and M.D. Craven, Appl. Phys. Lett. **109**, 033504 (2016).
[59] A. David, M.J. Grundmann, J.F. Kaeding, N.F. Gardner, T.G. Mihopoulos, and M.R. Krames, Appl. Phys. Lett. **92**, 053502 (2008).
[60] A. Rashidi, M. Monavarian, A. Aragon, and D. Feezell, Appl. Phys. Lett. (Submitted).
[61] D. Feezell and S. Nakamura, Comptes Rendus Phys. **19**, 113 (2018).
[62] J. Piprek, Phys. Status Solidi A **207**, 2217 (2010).
[63] N.F. Gardner, G.O. Müller, Y.C. Shen, G. Chen, S. Watanabe, W. Götz, and M.R. Krames, Appl. Phys. Lett. **91**, 243506 (2007).
[64] Y.C. Shen, G.O. Mueller, S. Watanabe, N.F. Gardner, A. Munkholm, and M.R. Krames, Appl. Phys. Lett. **91**, 141101 (2007).
[65] J. Iveland, L. Martinelli, J. Peretti, J.S. Speck, and C. Weisbuch, Phys. Rev. Lett. **110**, 177406 (2013).
[66] J. Hader, J.V. Moloney, and S.W. Koch, Appl. Phys. Lett. **99**, 181127 (2011).
[67] D.-S. Shin, D.-P. Han, J.-Y. Oh, and J.-I. Shim, Appl. Phys. Lett. **100**, 153506 (2012).
[68] M.-H. Kim, M.F. Schubert, Q. Dai, J.K. Kim, E.F. Schubert, J. Piprek, and Y. Park, Appl. Phys. Lett. **91**, 183507 (2007).
[69] M.F. Schubert, J. Xu, Q. Dai, F.W. Mont, J.K. Kim, and E.F. Schubert, Appl. Phys. Lett. **94**, 081114 (2009).
[70] P. Kivisaari, T. Sadi, J. Li, P. Rinke, and J. Oksanen, Adv. Electron. Mater. **3**, 1600494 (2017).
[71] Ü. Özgür, X. Ni, X. Li, J. Lee, S. Liu, S. Okur, V. Avrutin, A. Matulionis, and H. Morkoc, Semicond. Sci. Technol. **26**, 014022 (2010).
[72] S.-H. Han, D.-Y. Lee, S.-J. Lee, C.-Y. Cho, M.-K. Kwon, S.P. Lee, D.Y. Noh, D.-J. Kim, Y.C. Kim, and S.-J. Park, Appl. Phys. Lett. **94**, 231123 (2009).
[73] J. Xu, M.F. Schubert, A.N. Noemaun, D. Zhu, J.K. Kim, E.F. Schubert, M.H. Kim, H.J. Chung, S. Yoon, and C. Sone, Appl. Phys. Lett. **94**, 011113 (2009).
[74] A. David and N.F. Gardner, Appl. Phys. Lett. **97**, 193508 (2010).
[75] A. David, C.A. Hurni, N.G. Young, and M.D. Craven, Appl. Phys. Lett. **109**, 033504 (2016).
[76] S. Okur, M. Nami, A.K. Rishinaramangalam, S.H. Oh, S.P. DenBaars, S. Liu, I. Brener, and D.F. Feezell, Opt. Express **25**, 2178 (2017).
[77] M. Monavarian, A. Rashidi, A. Aragon, S.H. Oh, M. Nami, S.P. DenBaars, and D. Feezell, Opt. Express **25**, 19343 (2017).
[78] M. Monavarian, A. Rashidi, A.A. Aragon, S.H. Oh, A.K. Rishinaramangalam, S.P. DenBaars, and D. Feezell, Appl. Phys. Lett. **112**, 041104 (2018).
[79] I. Esquivias, S. Weisser, B. Romero, J.D. Ralston, and J. Rosenzweig, IEEE J. Quantum Electron. **35**, 635 (1999).
[80] A. David and M.J. Grundmann, Appl. Phys. Lett. **96**, 103504 (2010).
[81] P.G. Eliseev, M. Osin'ski, H. Li, and I.V. Akimova, Appl. Phys. Lett. **75**, 3838 (1999).
[82] H. Zhao, G. Liu, R.A. Arif, and N. Tansu, Solid-State Electron. **54**, 1119 (2010).
[83] J. Piprek and S. Li, Opt. Quantum Electron. **42**, 89 (2010).
[84] J. Piprek, Appl. Phys. Lett. **107**, 031101 (2015).
[85] D.S. Meyaard, G.-B. Lin, Q. Shan, J. Cho, E. Fred Schubert, H. Shim, M.-H. Kim, and C. Sone, Appl. Phys. Lett. **99**, 251115 (2011).

[86] C.-C. Pan, S. Tanaka, F. Wu, Y. Zhao, J.S. Speck, S. Nakamura, S.P. DenBaars, and D. Feezell, Appl. Phys. Express **5**, 062103 (2012).
[87] D.S. Meyaard, Q. Shan, Q. Dai, J. Cho, E.F. Schubert, M.-H. Kim, and C. Sone, Appl. Phys. Lett. **99**, 041112 (2011).
[88] V.A. Smagley, P.G. Eliseev, and M. Osinski, in *Phys. Simul. Optoelectron. Devices V* (International Society for Optics and Photonics, 1997), pp. 129–141.
[89] A. Rashidi, M. Monavarian, A. Aragon, A. Rishinaramangalam, and D. Feezell, IEEE Electron Device Lett. **39**, 520 (2018).
[90] A. Rashidi, M. Monavarian, A. Aragon, and D. Feezell, Appl. Phys. Lett. **113**, 031101 (2018).
[91] A. McAllister, D. Bayerl, and E. Kioupakis, Appl. Phys. Lett. **112**, 251108 (2018).
[92] E.F. Schubert, *Light-Emitting Diodes* (E. Fred Schubert, 2018).
[93] H.P.T. Nguyen, M. Djavid, K. Cui, and Z. Mi, Nanotechnology **23**, 194012 (2012).
[94] E. Kioupakis, Q. Yan, D. Steiauf, and C.G. Van de Walle, New J. Phys. **15**, 125006 (2013).
[95] I.E. Titkov, S.Y. Karpov, A. Yadav, V.L. Zerova, M. Zulonas, B. Galler, M. Strassburg, I. Pietzonka, H.-J. Lugauer, and E.U. Rafailov, IEEE J Quantum Electron **50**, 911 (2014).
[96] E. Kioupakis, P. Rinke, K.T. Delaney, and C.G. Van de Walle, Appl. Phys. Lett. **98**, 161107 (2011).
[97] J.-W. Shi, K.-L. Chi, J.-M. Wun, J.E. Bowers, Y.-H. Shih, and J.-K. Sheu, IEEE Electron Device Lett. **37**, 894 (2016).
[98] J.-W. Shi, H.-W. Huang, F.-M. Kuo, W.-C. Lai, M.-L. Lee, and J.-K. Sheu, IEEE Trans. Electron Devices **58**, 495 (2011).
[99] Y.C. Shen, J.J. Wierer, M.R. Krames, M.J. Ludowise, M.S. Misra, F. Ahmed, A.Y. Kim, G.O. Mueller, J.C. Bhat, and S.A. Stockman, Appl. Phys. Lett. **82**, 2221 (2003).
[100] M. Monavarian, A. Rashidi, A.A. Aragon, M. Nami, S.H. Oh, S.P. DenBaars, and D. Feezell, Appl. Phys. Lett. **112**, 191102 (2018).